Spectral correction of turbulent energy damping on wind LiDAR measurements due to ~~range-gate~~ spatial averaging

Matteo Puccioni and Giacomo Valerio Iungo

Wind Fluids and Experiments (WindFluX) Laboratory, Mechanical Engineering Department, The University of Texas at Dallas, 800 W Campbell Rd, 75080 Richardson, Texas, USA

Correspondence: Giacomo Valerio Iungo (valerio.iungo@utdallas.edu)

Abstract. Continuous advancements in pulsed wind LiDAR technology have enabled compelling wind turbulence measurements within the atmospheric boundary layer with ~~range gates~~ probe lengths shorter than 20 m and sampling frequency of the order of 10 Hz. However, estimates of the radial velocity from the back-scattered ~~laser beam~~ LiDAR signal are inevitably affected by an averaging process within each ~~range gate~~ probe volume, generally modeled as a convolution between the true velocity projected along the LiDAR line-of-sight and an unknown weighting function representing the energy distribution of the laser pulse along the ~~range gate~~ probe length. As a result, the spectral energy of the turbulent velocity fluctuations is damped within the inertial sub-range, thus not allowing to take advantage of the achieved spatio-temporal resolution of the LiDAR technology. In this article, we propose to correct this turbulent energy damping on the LiDAR measurements by reversing the effect of a low-pass filter, which can be estimated directly from the ~~LiDAR measurements~~ power spectral density of the along-beam velocity component. LiDAR data acquired from three different field campaigns are analyzed to describe the proposed technique, investigate the variability of the filter parameters and, for one dataset, assess the procedure for spectral LiDAR correction against sonic anemometer data. It is found that the order of the low-pass filter used for modeling the energy damping on the LiDAR velocity measurements has negligible effects on the correction of the second-order statistics of the wind velocity. In contrast, the cutoff ~~frequency~~ wavenumber plays a significant role in the spectral correction encompassing the smoothing effects connected with the LiDAR ~~gate~~ probe length. Furthermore, ~~the underestimation of the turbulence intensity modeled through the proposed filter is found to have a more pronounced effect for velocity acquisitions closer to the ground~~ the variability of the spatial averaging on wind LiDAR measurements is investigated for different wind speed, turbulence intensity, and sampling height. The results confirm that the effects of spatial averaging are enhanced with decreasing wind speed, smaller integral length scale and, thus, for smaller sampling height.

1 Introduction

Over the last decades, wind Doppler Light Detection and Ranging (LiDAR) technology has provided compelling features to perform wind turbulence measurements within the atmospheric boundary layer (ABL) for different scientific and industrial pursuits, such as air quality, meteorology (Spuler and Mayor , 2005; Emeis et al. , 2007; Bodini et al. , 2017), aeronautic transportation, and wind energy (Frehlich and Kelley , 2008; Zhan et al. , 2019). In the context of ABL turbulence, scanning

Doppler wind LiDARs were assessed against other measurement techniques, such as sonic anemometers and scanning Doppler wind radars, during the eXperimental Planetary boundary layer Instrumentation Assessment (XPIA) campaign (Lundquist et al. , 2017; Debnath et al. , 2017a, b; Choukulkar et al. , 2017; Debnath , 2018).

Different scanning strategies can be designed to characterize different properties of the ABL velocity field through LiDAR measurements (Sathe and Mann , 2013), while the highest spectral resolution is achievable by maximizing the sampling frequency and measuring over a fixed line-of-sight (LOS). Provided the use of a probe length, l, sufficiently small to probe the inertial sublayer at a height from the ground z, e.g. $l < 2\pi z$ according to Banerjee et al. (2015), turbulence statistics of the wind velocity field can be retrieved through fixed scans while providing a spectral characterization of the inertial sub-layer (Iungo et al. , 2013) ~~and very large coherent structures present within the ABL~~. 3D fixed-point measurements can be performed by retrieving the radial velocity measured simultaneously by three or more LiDARs intersecting at a fixed position (Mann et al. , 2009; Mikkelsen et al. , 2008; Carbajo et al. , 2014). In Mann et al. (2009), auto- and cross-spectral densities for the three velocity components were estimated through multiple scanning-LiDAR measurements. ~~Other turbulence statistics can also be evaluated through multiple scanning LiDARs, such as turbulent momentum fluxes~~ (Mann ~~et al.~~ , 2009)

Besides the easier deployment compared to the installation of classical meteorological towers, wind LiDARs tailored for investigations on atmospheric-turbulence currently provide probe volumes ~~, denoted as range gates,~~ smaller than 20 m along the direction of the laser beam and sampling frequency higher than 1 Hz, which are welcomed features for studies on ABL turbulence.

A Doppler wind LiDAR allows probing the atmospheric wind field utilizing a laser beam, ~~which~~ whose light is back-scattered in the atmosphere due to the presence of particulates suspended in the ABL. The velocity component along the laser-beam direction, denoted as radial or LOS velocity, is evaluated from the Doppler shift ~~on~~ of the back-scattered signal. A pulsed Doppler wind LiDAR, like those used for the present work, emits laser pulses to perform quasi-simultaneous wind measurements at multiple distances from the LiDAR as the pulses travel in the atmosphere. The wind measurements performed over each ~~range gate~~ probe volume can be considered as the convolution of the actual wind velocity field projected along the laser-beam direction with a weighting function representing the radial distribution of the energy associated with each laser pulse. Therefore, LiDAR measurements can be considered as the result of a low-pass filtering of the actual velocity field, where the characteristics of the low-pass filter are functions of the energy distribution of the laser pulse over the ~~range gate~~ probe volume, probe length ~~of the range gate~~ and accumulation time (Sjöholm et al. , 2009; Held and Mann , 2018).

A reduced variance of the wind velocity is generally measured with a Doppler wind LiDAR compared with that measured through a sonic anemometer due to the laser-pulse averaging and different size of the measurement volume. For single-point measurements performed with a Windcube 200S LiDAR and azimuth angle of the laser beam set equal to the mean wind direction, a variance reduction of 8% was ~~quantified for a gate length of 25 m, while it increased up to 20% for a probe length of 100 m~~ predicted for a gate length of 25 m, while it was increased up to 20% for a gate length of 100 m (Cheynet et al. , 2017).

Attenuation of the measured turbulent kinetic energy due to the averaging over each probe volume has been recovered through a spectral transfer function introduced in Mann et al. (2009). For fixed scans, by leveraging the Taylor's frozen-

turbulence hypothesis (Taylor , 1938; Panofsky and Dutton , 1984), the velocity energy spectrum is recovered through the deconvolution of the radial velocity with the weighting function representing the energy of the laser pulse. The critical part of this correction method consists of the empirical definition of the weighting function and its representative length scale (Banakh and Werner , 2005; Lindelöw , 2008; Mann et al. , 2009). As it will be shown in this paper, corrections performed through this deconvolution procedure often do not provide a satisfactory accuracy for wind turbulence measurements.

In this work, a procedure to correct the damping of turbulent kinetic energy associated with wavelengths comparable to the LiDAR ~~range gate~~ probe length is proposed. This procedure is based on inverting the effects of a low-pass filter, whose characteristics are directly determined by the power spectral density (PSD) of the LiDAR measurements. The remainder of this paper is organized as follows: the theoretical aspects of the correction procedure are discussed in §2, while in §3 the experimental campaigns performed to collect the various LiDAR datasets are described. In §4, an assessment of the proposed correction procedure is performed against sonic anemometry, while in §5 the correction procedure is tested for various LiDAR datasets. In §6, the spatial-averaging effects are investigated by varying the friction velocity, aerodynamic roughness length, and sampling height, thus for different mean wind speed and standard deviation ~~the relative importance of each low-pass filter's parameter is explored, first for a single synthetically-generated turbulence spectrum and then for a vertical array of them~~. Finally, concluding remarks are reported in §7.

2 Correction procedure for the LiDAR velocity spectra

Surface-layer scaling is typically used for spectral models of the wind speed assuming that the velocity integral length-scale is proportional to the height from the ground, z, and the Reynolds stresses can be normalized with the square of the friction velocity, u_τ.~~In this work, S_u is the PSD of the streamwise velocity and A_f and B_f are parameters estimated through best-fitting of the pre-multiplied energy spectra of the LiDAR velocity signals with Eq.~~1. ~~The term ϕ_ϵ (≥ 1) represents a dimensionless dissipation for non-neutral atmospheric stability regimes, with ϕ_ϵ equal to 1 for neutrally-stratified surface-layer flows (Kaimal et al. , 1972). For this work, we only consider near-neutral atmospheric conditions and slight variations connected with atmospheric stability are embedded in the coefficient A_f of Eq.~~ 1. A classical approach to model the power spectral density of the streamwise velocity, S_u, is the following:

$$\frac{f\,S_u(f)}{u_\tau^2\,\phi_\epsilon} = \frac{A\,n}{(1+B\,n)^{5/3}}, \tag{1}$$

where f is frequency, $n = fz/U$ is the reduced frequency, U is the mean advection velocity, and A and B are parameters estimated through the best-fitting of the pre-multiplied energy spectra of the LiDAR velocity signals with Eq. 1. The term ϕ_ϵ (≥ 1) represents a dimensionless dissipation for non-neutral atmospheric stability regimes, with ϕ_ϵ equal to 1 for neutrally-stratified surface-layer flows (Kaimal et al. , 1972). For this work, we only consider near-neutral atmospheric conditions and slight variations connected with atmospheric stability are embedded in the coefficient A. ~~The wind velocity spectra can also be modeled as a function of the non-dimensional frequency $n = fz/U$ (U is the local average horizontal wind speed), as follows~~: The spectral model of Eq. 1 is typically referred to as blunt model (Olesen et al. , 1984) or Kaimal model (Kaimal et al. , 1972;

IEC , 2007; Worsnop et al. , 2017; Risan et al. , 2018), and the parameter A is typically assumed equal to 105 (Kaimal et al. , 1972), later revised to 102 (Kaimal and Finnigan , 1994), and B equal to 33. It is noteworthy that within the inertial sub-layer, the pre-multiplied spectra scale as $n^{-2/3}$, while the maximum value occurs for a reduced frequency equal to $1.5/B$, which corresponds to the wavenumber $k_p = 3\pi/(B\ z)$ ~~(non-dimensional frequency of $1.5/B_n$)~~.

Considering the Cartesian reference frame, (x_1, x_2, x_3), where the coordinates are aligned with streamwise, transverse and vertical directions, respectively, the wind speed measured by a pulsed Doppler wind LiDAR can be modeled as the convolution between the projection of the wind velocity $\mathbf{u} = (u_1, u_2, u_3)$ along the laser-beam direction, $\mathbf{n} = (n_1, n_2, n_3)$, with a weighting function, ϕ, representing the energy distribution of the laser pulse within a ~~range gate~~ probe volume (Sjöholm et al. , 2009; Mann et al. , 2009; Cheynet et al. , 2017):

$$v_r(x) = \int_{-l/2}^{l/2} \phi(s)\ \mathbf{u}(s\mathbf{n} + x) \cdot \mathbf{n} ds, \tag{2}$$

where v_r is the radial or line-of-sight velocity measured along the laser-beam direction, $\mathbf{n}$, at a radial distance x from the LiDAR. The probe length ~~of the range gate~~ is l, while s is the radial position within the considered ~~gate~~ probe volume. The weighting function, ϕ, is normalized to unit integral. If the Doppler frequency is determined as the first moment of the signal PSD with the background subtracted appropriately, then the weighting function can be expressed as (Banakh and Werner , 2005; Mann et al. , 2009; Cheynet et al. , 2017):

$$\phi_1(s) = \frac{l - |s|}{l^2} \tag{3}$$

For the LiDAR Windcube 200S, the following weighting function can also be used (Lindelöw , 2008; Mann et al. , 2009):

$$\phi_2(s) = \frac{3(l - |s|)^2}{2l^3} \tag{4}$$

In the spectral domain, the Fourier transform of Eq. (3) is:

$$\varphi_1 = \frac{\sin^2(0.5kl)}{(0.5kl)^2}, \tag{5}$$

while for Eq. 4 is:

$$\varphi_2 = \frac{6}{(kl)^2} \cdot \left[1 - \frac{\sin(kl)}{kl}\right], \tag{6}$$

where $k = 2\pi f/U$ is the wavenumber evaluated through the Taylor's frozen-turbulence hypothesis (Taylor , 1938). As shown in Mann et al. (2009), the measured velocity spectrum, S_L, can be modeled as:

$$S_L(k_1) = n_i n_j \int_{-\infty}^{+\infty}\int_{-\infty}^{+\infty} |\varphi(\mathbf{k}\cdot\mathbf{n})|^2 \Phi_{ij}(\mathbf{k}) dk_2 dk_3, \tag{7}$$

where: $\mathbf{k} = (k_1, k_2, k_3)$ is the wavenumber vector and summation over repeated indices is assumed. In Eq. 7 , $\Phi_{ij}(\mathbf{k})$ is the spectral tensor obtained as Fourier transform of the Reynolds stress tensor and $\varphi(\mathbf{k}\cdot\mathbf{n})$ is the Fourier transform of the convolution function. When the laser beam stares along the mean wind direction with a relatively low elevation angle, namely

with $\mathbf{n} \approx (1,0,0)$, the PSD of the radial velocity, S_L, is equal to the product between the spectrum of the actual radial velocity, $\hat{S}_L(k_1)$, and the square of the Fourier transform of the weighting function, $\varphi(k_1)$:

$$S_L(k_1) = \int_{-\infty}^{+\infty}\int_{-\infty}^{+\infty} |\varphi(k_1)|^2 \Phi_{ij}(\mathbf{k}) dk_2 dk_3 = |\varphi(k_1)|^2 \hat{S}_L(k_1). \tag{8}$$

Equation 8 shows that the spectrum of the measured radial velocity, S_L, is equal to the true velocity spectrum, $\hat{S}_L$, low-pass filtered with a certain transfer function. In this work, the latter is modeled as:

~~$|\tilde{\varphi}|^2(f) = \left[1 + \left(\frac{f}{f_{Th}}\right)^{\alpha}\right]^{-1}$,~~

$$|\tilde{\varphi}|^2(k) = \left[1 + \left(\frac{k}{k_{Th}}\right)^{\alpha}\right]^{-1}, \tag{9}$$

where α and ~~f_{Th}~~ k_{Th} represent the order and cutoff ~~frequency~~ wavenumber, respectively, of a low-pass filter (Ogata , 2010). The symbol $\tilde{}$ is used to differentiate the analytical model of the low-pass filter from its empirical estimate through the ratio between the fitted Kaimal spectrum and the PSD of the LiDAR velocity, φ_*^2. These features of the low-pass filter and, thus, of the LiDAR measuring process, are functions of the LiDAR ~~range gate~~ probe length, the elevation angle of the laser beam, the relative angle between wind direction and azimuth angle of the laser beam, accumulation time, and characteristics of the laser pulse. Therefore, it is highly challenging to predict these parameters a priori, while it ~~seems more efficient~~ advisable to estimate α and ~~f_{Th}~~ k_{Th} directly from the specific LiDAR data under analysis. To this aim, we propose the following iterative procedure to correct the effects of the spatial averaging on wind LiDAR measurements, which is summarized in the flow chart of Fig. 1.

First, the pre-multiplied spectrum of the radial velocity projected in the horizontal mean wind direction is fitted with the ~~Kaimal~~ spectral model of Eq. 1 only for ~~frequencies~~ wavenumbers smaller than ~~f_{Th}~~ $k_{Th,0} = 2\pi/l$. Indeed, we expect to observe significant spatial-averaging effects for turbulent length scales smaller than the probe length, l. ~~As it will be shown in the following, f_{Th} is determined iteratively and is of the order of $\mathcal{O}(10^{-1})$ Hz.~~ For ~~frequencies~~ wavenumbers higher than ~~f_{Th}~~ the selected cutoff value, the ratio between the fitted Kaimal spectrum and the PSD of the LiDAR velocity, φ_*^2, is calculated to quantify the effect of the energy damping due to the LiDAR measuring process. Subsequently, the LiDAR-to-Kaimal ratio, φ_*^2, is fitted with Eq. 9 through a least-square algorithm to estimate the filter order, α, and provide an updated value for the cutoff ~~frequency~~ wavenumber, ~~f_{Th}~~ k_{Th}. ~~If the guessed cutoff frequency is larger than the fitted value, the fitting of the LiDAR spectrum with the Kaimal model is repeated updating the value of cutoff frequency. Conversely, if the cutoff frequency calibrated on the LiDAR-to-Kaimal ratio is larger than the guessed value,~~ This process is iterated until convergence on the parameter k_{Th} is achieved (for this work, the convergence condition imposed is a variation of k_{Th} smaller than 1% of the previous value). If during the iterative process, k_{Th} achieves a value equal or smaller than that corresponding to the spectral peak, k_p, then the procedure is arrested and a warning is dispatched indicating that the correction procedure was not successful. This warning condition never occurred for all the data analyzed in this work. Furthermore, it should be considered that when k_{Th} achieves

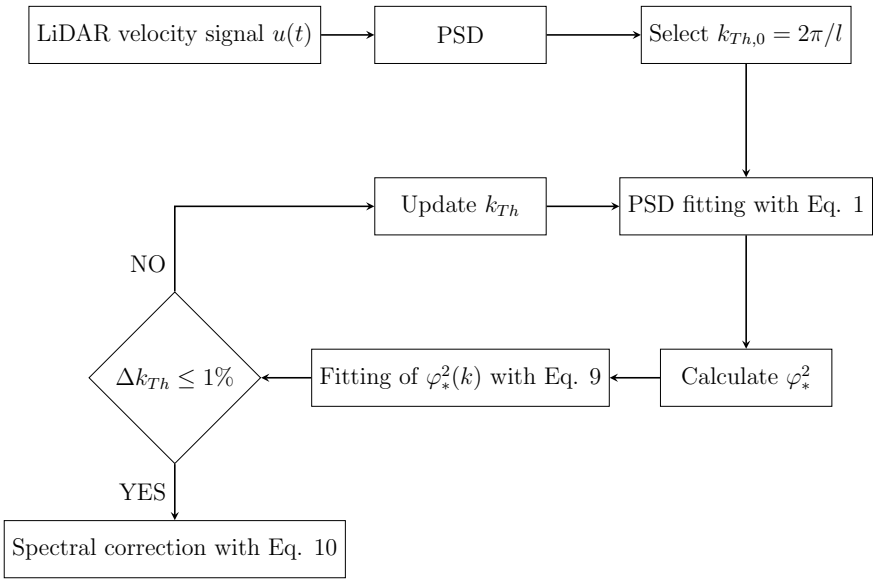

Figure 1. Flowchart for the iterative correction procedure of the LiDAR velocity measurements.

values close to k_p, the part of the velocity spectrum, S_u, used for the fitting procedure with Eq. 1 can be so limited to jeopardize the accuracy of the fitting procedure. Once convergence in k_{Th} is achieved, the corrected velocity spectrum, ~~$\tilde{S}_L(f)$~~ $\tilde{S}_L(k)$, is calculated as:

~~$\tilde{S}_L(f) = \frac{S_L(f)}{\tilde{\varphi}^2(f)}$~~.

$$\tilde{S}_L(k) = \frac{S_L(k)}{\tilde{\varphi}^2(k)}. \tag{10}$$

It is noteworthy that in contrast to existing models using pre-defined functions to correct the energy damping of the velocity fluctuations, see e.g. Eqs. 5 and 6 (Cheynet et al. , 2017; Sjöholm et al. , 2009), the proposed procedure calculates the characteristics of the damping on the LiDAR velocity signals directly from the experimental data, which leads, as it will be shown in the following, to enhanced accuracy in the correction of the LiDAR velocity spectra.

3 Experimental Setup and selected LiDAR datasets

The present study is based on wind LiDAR measurements collected from three different experimental campaigns. The first dataset was acquired during the period June 9-24, 2018 at the Surface Layer Turbulence and Environmental Science Test (SLTEST), which is part of the U.S. Dugway Proving Ground facility in Utah (GPS location: $40°08'07"N, 113°27'04"W$,

UTC offset -6 h). Characterized by an elevation variability of 1 m every 13 km (Kunkel and Marusic , 2006; Metzger and Klewicki , 2001), this facility is located in the South West of the Great Salt Lake and extends for 240 km and 48 km along North-South and East-West directions, respectively. An aerial view of the SLTEST facility is reported in Fig. 2a. During the experiment, the prevailing wind direction was from North-North-East.

The second field campaign was carried out at a test site in Celina, TX (GPS location: $33°17'35.3"$N, $96°49'17.5"$W, UTC offset -5 h), which is a relatively flat terrain with a certain variability in land cover (Fig. 2b). For these two field campaigns, wind velocity measurements were performed with a Streamline XR scanning Doppler pulsed wind LiDAR manufactured by Halo Photonics, whose technical details are reported in Table 1. LiDAR fixed scans were performed with an elevation angle between $1.98°$ and $10°$, while the azimuth angle was set equal to the mean wind direction. The latter was monitored through Vertical Azimuth Display (VAD) scans with an elevation of $25°$ and a sampling period of about 90 s, or through Doppler Beam Swinging (DBS) scans. DBS or VAD scans were executed hourly to monitor variations in the mean wind direction, while the azimuth angle for the fixed scans was updated automatically at the end of each DBS or VAD scan through the feedback scan mode embedded in the LiDAR software, and using the wind-direction measured at the height of 53 m. ~~For the fixed scans, the sampling frequency was varied between 0.5 and 3.3 Hz, while the probe length was always set equal to 18 m.~~ To investigate possible variations of the averaging process related to the accumulation time, the sampling frequency of the fixed scans was varied between 0.5 Hz and 3.3 Hz, while the range gate was always set equal to 18 m.

The third campaign considered in this study is the eXperimental Planetary boundary layer Instrumentation Assessment (XPIA), performed during the period March 2 - May 31, 2015 at the Boulder Atmospheric Observatory (BAO) research facility in Erie, Colorado. For the XPIA campaign, twelve Campbell CSAT3 3D sonic anemometers were mounted on the BAO meteorological tower at heights of 50 m, 100 m, 150 m, 200 m, 250 m and 300 m above the ground. Each height was monitored with two sonic anemometers pointing towards North-West and South-East, respectively. Three velocity components and temperature were recorded with a sampling rate of 20 Hz. For a complete description of the scanning strategies and the

Figure 2. Aerial views of the test sites: **(a)** SLTEST facility; **(b)** Celina site; **(c)** XPIA campaign at the Boulder Atmospheric Observatory. Source of Google Earth. Black crosses represent the instrument locations. In **(c)**, each LiDAR is labeled with its respective name.

Table 1. Technical specifications of the pulsed scanning Doppler wind LiDARs used for this work, namely a Streamline XR by Halo Photonics and a Windcube 200S by Leosphere.

Parameter	Value	
LiDAR	Streamline XR	Windcube 200S
Wavelength [μm]	1.5	1.54
Repetition rate [kHz]	10	10
Velocity resolution [m s^{-1}]	± 0.0764	< 0.5
Velocity bandwidth [m s^{-1}]	± 38	± 30
Number of FFT points	1024	1024
Measurement range	45 m to 12 km	50 m to 6 km
LiDAR gate length	18 m to 120 m	25 m to 100 m
Number of gates	200	200
Sampling rate	0.5 Hz to 4 Hz	0.1 Hz to 2 Hz

instruments utilized during the XPIA experiment see Lundquist et al. (2017). Fig. 2(c) shows the locations of the ~~used~~ LiDARs used.

In the present study, from the XPIA experiment we focus on tests performed during the period March 21-24, 2015 with a Windcube 200S scanning Doppler pulsed wind LiDAR manufactured by Leosphere. Technical specifications of the Windcube 200S wind LiDAR are reported in Table 1. The LiDAR performed measurements by staring towards one of the sonic anemometers for a period of 14.5 minutes. A sequential scan at four different heights was done for every hour during each day; details of these tests are available in Debnath (2018). Simultaneous measurements performed with a scanning Doppler wind LiDAR and sonic anemometers are analyzed to assess the proposed spectral correction procedure of LiDAR measurements.

For the Celina and SLTEST field campaigns, the regime of the ~~static~~ atmospheric stability was monitored through sonic anemometers mounted at a height of 3 m in the proximity of the LiDAR location. The sampling frequency of the sonic anemometer data was 20 Hz, while atmospheric stability was characterized through the Obukhov length calculated as follows (Monin and Obukhov , 1954):

$$L = -\frac{\theta_v u_{\tau,S}^3}{\kappa g \overline{w'\theta_v'}}, \tag{11}$$

where $\kappa = 0.41$ is the von Kármán constant, g is the gravitational acceleration, $\overline{w'\theta_v'}$ is the sensible heat flux, θ_v is the average virtual potential temperature (in Kelvin) and $u_{\tau,S}$ is the friction velocity calculated from sonic anemometer data as (Stull , 1988):

$$u_{\tau,S} = \left(\overline{u'w'}^2 + \overline{v'w'}^2\right)^{1/4}. \tag{12}$$

To avoid effects of thermal stratification and buoyancy on our analysis, only datasets acquired under near-neutral conditions are considered, which are selected by imposing the threshold: $|z/L| \leq 0.05$ (Kunkel and Marusic , 2006; Liu et al. , 2017).

The LiDAR velocity signals undergo a quality control process to ensure statistical significance and accuracy of the measurements. ~~For the SLTEST and Celina campaigns, LiDAR fixed scans were performed with the laser beam aligned in the mean wind direction, which is monitored hourly through DBS or VAD scans~~. Only datasets with a variability of the 10-minute averaged wind direction within the range $\pm 20^\circ$ have been considered to avoid significant offset between the LiDAR azimuth angle and the instantaneous wind direction (Hutchins et al. , 2012).

The quality of the LiDAR signals is then checked based on the intensity of the back-scattered signal. For the Windcube 200S LiDAR, the samples with a carrier-to-noise ratio (CNR) higher than -25 dB are selected, while for the Streamline XR LiDAR data are analyzed only if the intensity of the back-scattered signal is higher than 1.01.

The statistical steadiness of the LiDAR signals is estimated through the non-stationary index (IST) calculated as follows (Liu et al. , 2017):

$$IST = \frac{CV_m - CV_{tot}}{CV_{tot}}, \tag{13}$$

where:

$$CV_m = \frac{1}{N}\sum_{j=1}^{N} CV_j. \tag{14}$$

In Eq. 14, CV_j is the variance of a signal subset with a duration of 5 minutes, while N is the total number of subset signals generated without overlapping; CV_{tot} is the variance of the signal over the entire period. For Celina and SLTEST campaigns, IST was calculated for 1-hour periods, while for the XPIA deployment the whole 14.5-minute record was analyzed. For quality control purpose, signals with $IST \geq 40\%$ are usually rejected (Foken et al. , 2004; Liu et al. , 2017). The IST is calculated for each range gate and the maximum IST value for the selected datasets is reported in the eighth column of Table 2.

Subsequently, a gradient-based procedure is used to remove outliers from the LiDAR radial velocity signals. Specifically, the partial derivative in time of the radial velocity is calculated through a second-order central finite-difference scheme, and velocity samples with absolute partial derivative larger than 15 times the respective median value calculated over the entire signal are marked as outliers and replaced through the inpaint-nans function available in Matlab (D'Errico , 2004). The used threshold value is selected based on a sensitivity analysis. ~~which are replaced through a least-squares approach in time for each LiDAR gate under investigation. Each signal is linearly detrended in time over the whole duration in order to remove large-scale fluctuation, while keeping turbulent velocity fluctuations.~~ Based on the above-mentioned quality-control procedure, five datasets were selected, whose details are reported in Table 2.

The radial velocity, V_r, measured by a Doppler wind LiDAR, as explained in §2, is expressed as:

$$V_r = V_h \cos(\theta - \theta_w)\cos\Phi + W\sin\Phi \tag{15}$$

where θ and Φ are the LiDAR azimuth and elevation angles, respectively, θ_w is the wind direction, V_h and W are the horizontal and vertical wind velocities, respectively. As previously mentioned, for the SLTEST and Celina field campaigns, LiDAR measurements were carried out with the azimuth angle equal to the mean wind direction and very low elevation angles (Table

Table 2. Description of the selected datasets: Φ is the LiDAR elevation angle, f_S is the sampling frequency, l is the probe length, IST is the maximum value of the non-stationary index, u_τ is the friction velocity and z_0 is the aerodynamic roughness length. The last column reports the symbol used for each dataset.

Date	Dataset	LiDAR	UTC Time	Φ [°]	f_s[Hz]	l[m]	max. IST [%]	u_τ [m s^{-1}]	z_0 [mm]	Symbol
23 March 2015	XPIA	Windcube	14:15 - 14:29	5.00	2	50	19.1	0.179	-	-
10 June 2018	SLTEST		10:00 - 13:00	3.50	1	18	24.6	0.414	$2.1 \cdot 10^{-2}$	×
26 May 2017	Celina1		23:35 - 00:35	10.00	3.3	18	24.1	0.479	15	●
02 October 2017	Celina2	Streamline	22:10 - 01:10	5.00	0.5	18	37.7	0.526	87	■
26 January 2018	Celina3		20:30 - 23:30	1.98	1	18	39.7	0.404	17	▼

2). Therefore, we can calculate an approximation of the horizontal wind speed as:

$$U_{eq} = V_r / \cos\Phi, \tag{16}$$

which is referred to as horizontal equivalent velocity. In the following U_{eq} is considered to calculate the streamwise velocity spectrum. Furthermore, the variance of the radial velocity is the first-order approximation of the streamwise-velocity variance given the above-mentioned setup constraints (Eberhard et al. , 1989; Sathe and Mann , 2013).

4 Assessment of the LiDAR spectral correction against sonic anemometry

In this section, the procedure proposed in §2 to correct the energy damping in the LiDAR velocity measurements due to the energy pulse distribution over the ~~range gate~~ probe volume is assessed against sonic anemometry by leveraging the XPIA dataset, whose characteristics are summarized in Table 2. LiDAR fixed scans were performed with an elevation angle of 5° to have one range gate in the proximity of a sonic anemometer installed on the BAO tower at a height of 100 m. The LiDAR ~~range gate~~ probe length used for that experiment was equal to 50 m, while the sampling rate was set equal to 2 Hz.

Based on the instantaneous wind direction measured by the sonic anemometer and neglecting the vertical velocity due to the very low elevation angle of the LiDAR laser beam, the horizontal equivalent velocity, U_{eq}, is calculated from the LiDAR radial velocity through Eq. 15 and it is reported in Fig. 3 with a blue line. The ~~PSD of the~~ LiDAR equivalent velocity, U_{eq}, is then high-pass filtered to remove low-frequency non-turbulent velocity fluctuations, using the following spectral transfer function:

$$G(k;\beta,k_{co}) = \frac{1+\tanh\left[\beta \cdot \log\left(\frac{k}{k_{co}}\right)\right]}{2}, \tag{17}$$

where k_{co} is the cutoff wavenumber, which should be smaller than k_p to avoid effects on the spectral peak. The parameter β is set equal to 100 to generate a sufficiently sharp filter across the cutoff wavenumber, k_{co} (Hu et al., 2019). The PSD of the velocity signal high-pass filtered with a cutoff wavenumber $k_{co} = 1.26 \times 10^{-3}$ m^{-1} is reported in Fig. 4(a) with a grey line.

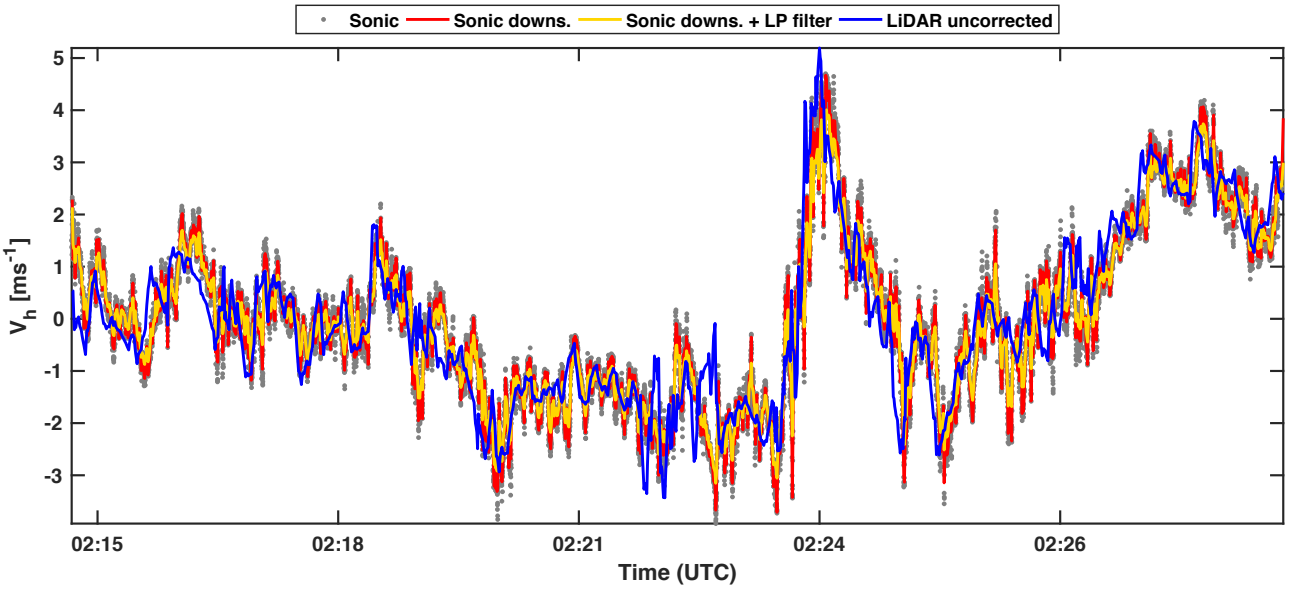

Figure 3. Subset of the horizontal velocity measured with a LiDAR and sonic anemometer from the XPIA dataset. The grey dots represent the original 20-Hz-sampled sonic-anemometer data; the red line is the sonic anemometer signal downsampled at 2 Hz; the yellow line is the sonic anemometer signal after the convolution of Eq. 9; the blue line is the LiDAR signal before the spectral correction.

In case significant noise in the velocity spectra is observed in the proximity of the Nyquist wavenumber, see e.g. Debnath (2018), as for this velocity signal, a denoising procedure is then applied to remove possible noise effects on the velocity signals. Following the wavelet-transform-based procedure proposed by To et al. (2009), the velocity signal is decomposed in a 10-level orthogonal wavelet basis. For each level, a soft-threshold selection is applied to the wavelet coefficients to remove those related to noise. The estimated noise-free wavelet coefficients, d_{jk}, are calculated as:

$$d_{jk} = \begin{cases} \text{sgn}(w_{jk})(|w_{jk}| - T_j) & \text{if } |w_{jk}| > T_j \\ 0 & \text{otherwise} \end{cases}, \tag{18}$$

where $j = 1, ..., 10$ is the number of levels in the wavelet basis; $k = 1, ..., 2^j$ and w_{jk} are the coefficients of the discrete wavelet transform of the original signal. T_j represents a noise-based threshold for the j^{th} level, that for this work is set to (To et al. , 2009):

$$T_j = \frac{\text{med}(|w_{jk}|)}{0.67} \cdot \sqrt{2 \log 2^j}, \tag{19}$$

where med$(\cdot)$ stands for the median value. Finally, the denoised signal is reconstructed in time through the modified wavelet coefficients d_{jk}. The spectrum of the denoised LiDAR velocity signal is reported in Fig. 4(a) with a light-blue line.

For modeling purpose, the velocity spectra are then smoothed in the wavenumber domain following the Savitztky-Golay filter (Savitzky and Golay , 1964), by using a second-order polynomial function and windows with the width equal to int$[10(160k)^{0.5}]$,

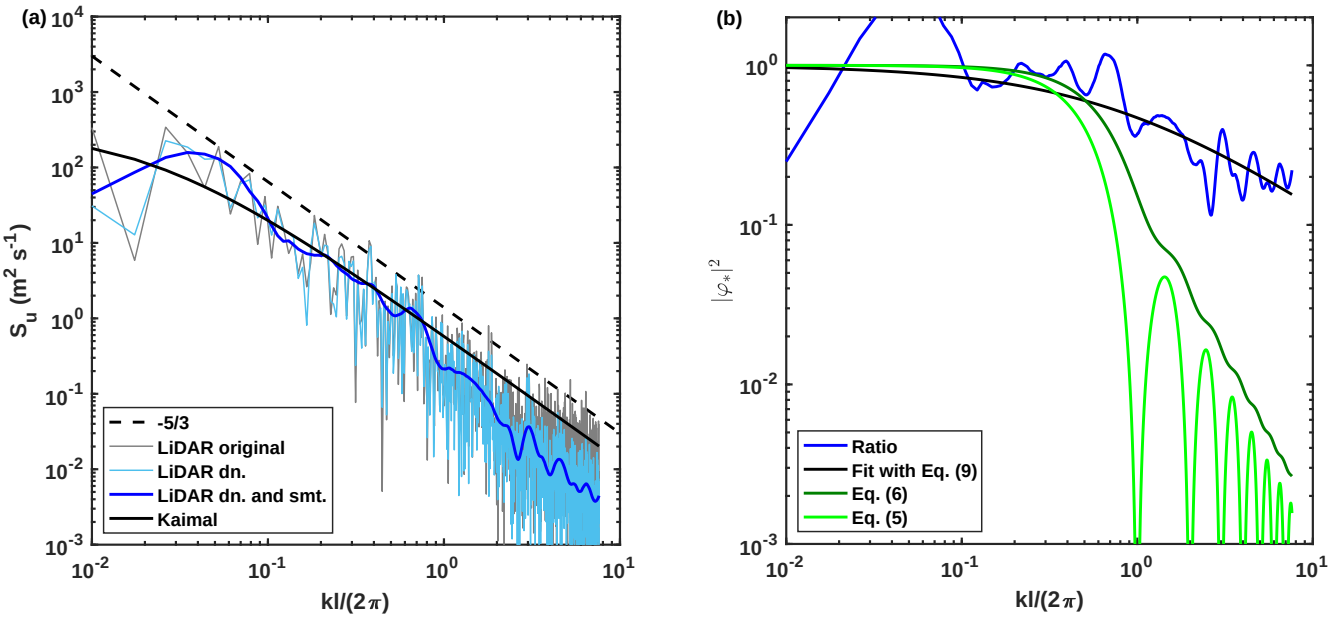

Figure 4. Correction of the LiDAR velocity spectrum from the XPIA dataset: **(a)** velocity spectra of the raw LiDAR data (grey), LiDAR data after application of the de-noising procedure (To et al. , 2009) (light blue), LiDAR data after smoothing procedure (dark blue), Kaimal spectrum tuned for $kl/(2\pi) \leq 0.4$ (black) and $-5/3$ slope (black dashed); **(b)** $|\varphi_*|^2$ (blue), $|\varphi_*|^2$ fitted with Eq. 9 (black); predictions from Eq. 5 (dark green) and Eq. 6 (bright green) are reported as well.

where k is in m^{-1} and int is rounding to the closest integer number (Balasubramaniam , 2005). ~~Specifically, the energy spectrum is smoothed with a moving average over intervals whose length increases with the frequency, followed by a best-fit with a second-order polynomial function.~~ The result is an increased level of smoothness moving towards the Nyquist ~~frequency~~ wavenumber. The LiDAR velocity spectrum resulting from the de-noising and smoothing procedures is reported in Fig. 4(a) with a blue line. The PSD of the LiDAR velocity is then fitted through the spectral model (Eq. 1) for wavenumbers $kl/(2\pi) \leq 0.4$ producing the following fitting parameters: ~~$A_f = 336.1$ s, $B_f = 355.3$ s,~~ $A = 23.3$, $B = 24.7$. The resulting Kaimal spectrum is plotted in Fig. 4(a) with a black line.

A deviation of the LiDAR velocity spectrum from the $-5/3$ scaling of the inertial sub-range is observed ~~for $kl/(2\pi) \gtrapprox 0.4$,~~ due to the LiDAR measuring process over the ~~range gate~~ probe volume. The ratio between the fitted Kaimal spectrum and the LiDAR velocity spectrum, $|\varphi_*|^2$ in Fig. 4(b), is then fitted with Eq. 9 to estimate the low-pass filter of order α and cutoff ~~frequency~~ wavenumber, ~~f_{Th}~~ k_{Th} . For this LiDAR velocity signal, α is equal to 0.774 and $k_{th}l/(2\pi) \approx 0.8$, with an R^2 value of 0.702, which confirms the proposed model is a good approximation for the damping of the velocity fluctuations over the LiDAR ~~range gate~~ probe volume. In Fig. 4(b), the weighting functions of Eqs. 5 and 6 are also reported for a ~~range gate~~ probe length l =50 m.

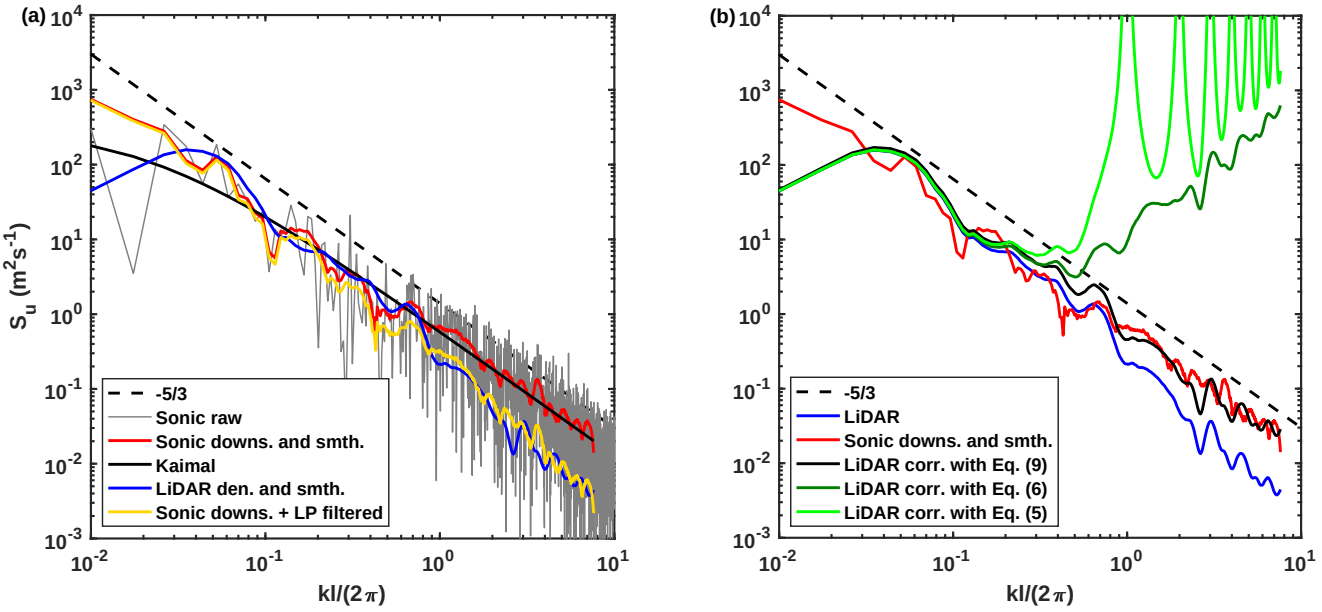

Figure 5. Comparison of LiDAR velocity data against sonic anemometry data for the XPIA dataset: **(a)** raw sonic anemometer data (grey), down-sampled and smoothed sonic-anemometer (red), Kaimal model (black) tuned on the LiDAR velocity spectrum (blue), sonic anemometer signal down-sampled and low-pass filtered (yellow); **(b)** LiDAR velocity spectrum (blue), down-sampled and smoothed sonic anemometer spectrum (red), LiDAR spectrum corrected with Eq. 9, 5 and 6 (black, dark and bright green lines, respectively).

To assess the accuracy of the estimated low-pass filter in representing the LiDAR averaging process over a ~~range gate~~ probe volume, first we apply the estimated low-pass filter to the simultaneous and co-located sonic anemometer velocity signal. The horizontal velocity retrieved from the sonic anemometer is first down-sampled with the sampling frequency of the LiDAR measurements, namely 2 Hz, using the Matlab function "decimate" with a finite-impulse response (FIR) low-pass filter with order equal to 10 (Weinstein , 1979). The resulting down-sampled velocity signal is reported with a red line in Fig. 3, and the respective PSD in Fig. 5(a). Subsequently, the down-sampled sonic-anemometer signal is low-pass filtered with the filter of Eq. 9 modeled only using the LiDAR data (yellow line in Fig. 3 and in Fig. 5(a)). The comparison in Fig. 3 of the sonic anemometer signal down-sampled and low-pass filtered with the LiDAR raw signal already highlights a very good agreement, which suggests that the energy damping carried out by the LiDAR pulse over the ~~range gate~~ probe volume is well represented through the proposed low-pass filter. This feature is further corroborated by the respective spectra reported in Fig. 5(a). Specifically, the ~~spectrum of the LiDAR signal~~ spectrum of the LOS velocity has the same slope in the inertial sub-range of the sonic-anemometer signal down-sampled and low-pass filtered, while some differences are observed for lower frequencies, which are most probably due to the different size of the measurement volume of the two instruments, namely 50 m for the LiDAR and 0.3 m for the sonic anemometer.

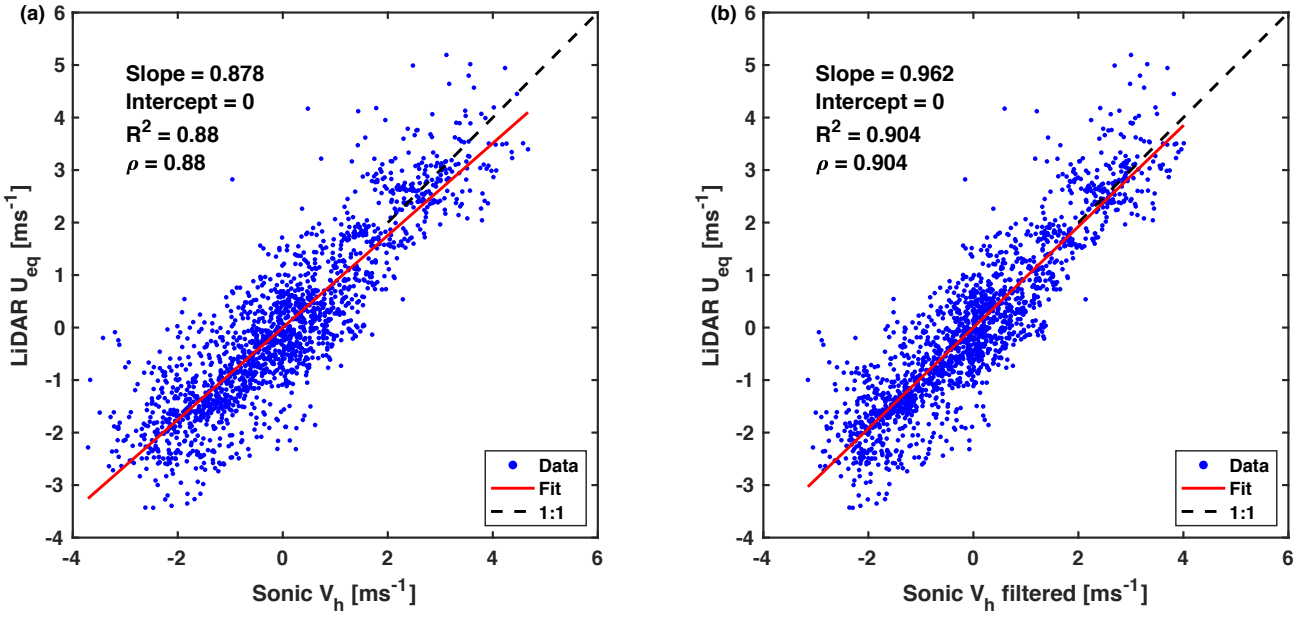

Figure 6. Linear regression between LiDAR horizontal equivalent velocity, U_{eq}, and sonic anemometer horizontal velocity from the XPIA dataset: **(a)** raw data from the sonic anemometer; **(b)** sonic anemometer data down-sampled and low-pass filtered.

The comparison between LiDAR and sonic anemometer data is now presented through a linear regression analysis, which is reported in Fig. 6. The LiDAR horizontal equivalent velocity, U_{eq}, is analyzed against the horizontal wind speed measured by the sonic anemometer before (Fig. 6(a)) and after (Fig. 6(b)) the low-pass filtering. All the linear regression parameters improve for the low-pass filtered sonic anemometer data: the slope increases from 0.878 to 0.962, the R-square value increases from 0.88 to 0.904, and the correlation coefficient, ρ, increases from 0.88 to 0.904.

We now aim to correct the LiDAR velocity signal from the energy damping due to the laser pulse distribution over the ~~range gate~~ probe volume. First, the LiDAR velocity spectrum is corrected by using the existing models of Eqs. 5 and 6 with $l = 50$ m, i.e. the used LiDAR ~~range gate~~ probe length. As shown in Figs. 4(b) and 5(b), these correction methods largely over-estimate the turbulent energy for ~~frequencies~~ wavenumbers larger than ~~f_{Th}~~ k_{Th} or, in other words, the characteristic length scale should be smaller than the LiDAR ~~range gate~~ probe length to provide reasonable spectral corrections. A possible explanation for the poor performance of these deconvolution models could be the different probe ~~gate~~ length used for the XPIA campaign ($l = 50$ m) in contrast to $l = 30$ m used in the original study of this deconvolution model (Mann et al. , 2009) , and the presence of measurement noise in the data, which is not accounted for in the models of Eqs. 5, 6.

According to the correction technique proposed in this paper, the LiDAR velocity spectrum can now be corrected for the averaging process by reversing the effect of the estimated low-pass filter through Eq. 10. The corrected velocity spectrum is reported in Fig. 5(b) with a black line. The velocity spectrum of the corrected LiDAR velocity signal clearly shows that the

expected slope of $-5/3$ in the inertial sub-range is recovered, while the spectral energy for ~~frequencies~~ lower wavenumbers ~~lower than f_{Th}~~ are practically unchanged.

~~To provide more insight on the temporal consistency between the corrected LiDAR time-series and the sonic anemometer data, we band-pass filter LiDAR and sonic anemometer data between the selected cutoff frequency $f_{th} = 0.04$ Hz ($kl/(2\pi) \approx 0.4$) and the Nyquist frequency of the LiDAR measurements, i.e. 1 Hz. Indeed, this is the frequency range more affected by the smoothing process over the probe volume and, thus, requiring more correction of the spectral energy. The filtered velocity signals are subdivided into sub-periods with duration $1/f_{th} = 25$ s, and the standard deviation of the wind velocity is calculated. The linear regression analysis of the velocity standard deviation calculated from the sonic anemometer data and the LiDAR data before and after the spectral correction (reported in Figs. 7(a) and (b), respectively) highlights the positive effect of the spectral correction on the second-order statistics of the LiDAR measurements. For the linear regression of the velocity standard deviation, after the spectral correction the slope increases from 0.674 to 1.083 and the intercept reduces from 0.132 to -0.022, while the remaining parameters are essentially unaltered.~~

5 Variability of the low-pass filter parameters

For the SLTEST and Celina field campaigns, LiDAR velocity measurements were collected for time periods between 2 and 3 hours (see Table 2). The procedure used to obtain the streamwise velocity spectrum is the following: for each LiDAR velocity signal, the high-pass filter of Eq. 17 is applied with a cutoff wavenumber $k_{co} = 0.001$ m^{-1} to remove low-frequency velocity fluctuations connected with atmospheric mesoscales. The PSD of each velocity signal is then calculated with the pwelch function implemented in Matlab (Welch , 1967) without window overlapping and window width corresponding to k_{co}. Subsequently, smoothing of the velocity spectra is carried out through the Savitzky-Golay filter, as detailed in the previous section (Savitzky and Golay , 1964; Balasubramaniam , 2005).

The ~~first- and second-order statistics~~ mean values and variance of the LiDAR equivalent velocity are plotted in Figs. 7(a) and (b), respectively. For the mean velocity field in Fig. 7(a), while a logarithmic region is generally observed at the lower heights, a noticeable difference in terms of terrain roughness between the SLTEST and Celina sites reflects in different vertical intercepts and respective aerodynamic roughness length. The latter is estimated to be equal to 0.021 mm for SLTEST and, as average, 37 mm for the Celina site.

~~The different surface roughness of the two sites also affects the variance of the equivalent horizontal velocity, which is~~ The vertical profiles of streamwise velocity variance are reported in Fig. 7(b) as a function of height. For the datasets collected at the Celina site, a general increase of the velocity variance is observed with increasing height. Specifically, for the dataset Celina1, after achieving a maximum value at height $z \geq 40$ m, a quasi-logarithmic reduction of the velocity variance is observed with increasing height, which is in agreement with previous laboratory and numerical studies of canonical boundary layer flows (Kunkel and Marusic , 2006; Meneveau and Marusic , 2013). A logarithmic reduction of the velocity variance with increasing height is also observed for the SLTEST dataset throughout the entire height-range.

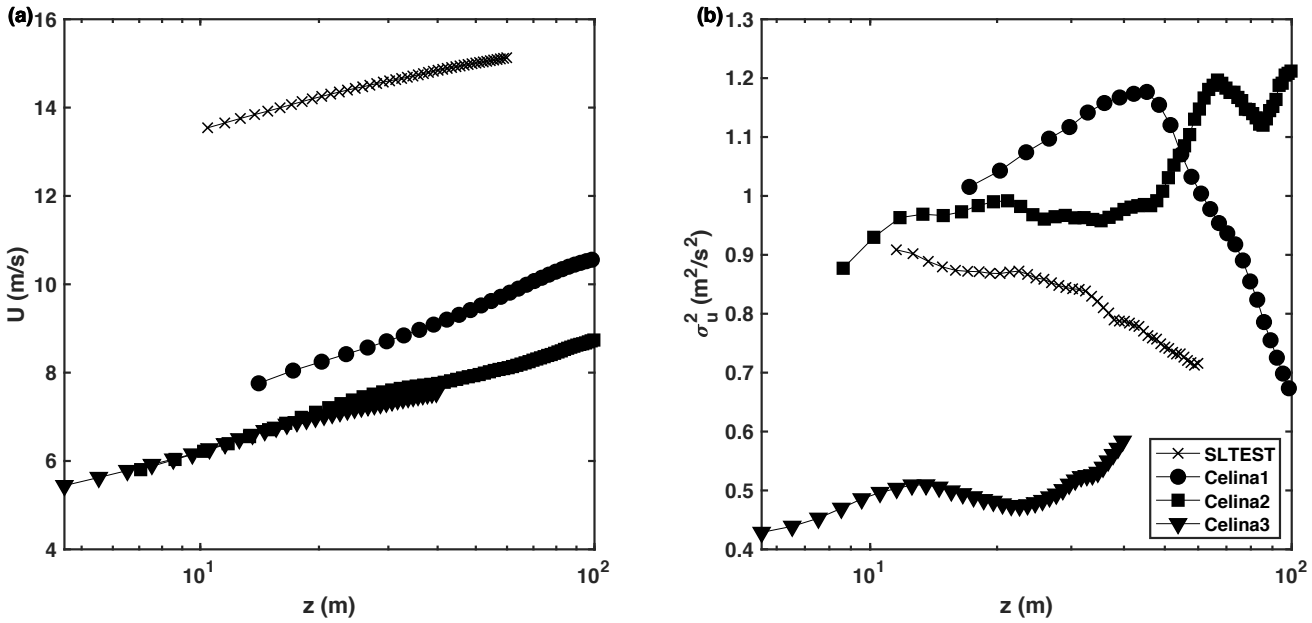

Figure 7. First- and second-order statistics of the equivalent velocity, U_{eq}, as a function of height for the various datasets: **(a)**: mean value; **(b)**: variance.

For the SLTEST dataset, the PSD of the LiDAR velocity signals acquired at the different gates from 10 m up to 60 m with a vertical spacing of 1 m are plotted in Fig. 8. A departure from the expected $-5/3$ slope in the inertial sub-range is observed ~~starting from $f \gtrapprox 0.1$ Hz~~ for wavenumbers larger than 0.07 m^{-1}. ~~Considering the observed spectral energy damping, the Kaimal model for the streamwise turbulence (Eq. 1) is fitted on the measured LiDAR velocity spectra only for frequencies with $f \lessapprox 0.1$Hz~~. The ~~fitted~~ Kaimal spectra, which are obtained by fitting the measured LiDAR velocity spectra only for wavenumbers lower than the respective k_{Th} for each height, are reported in Fig. 9(a) for the lowest and highest range gates. The ratio between the LiDAR and Kaimal spectra, $|\varphi_*|^2$, is then calculated and fitted through Eq. 9 to estimate the order and cutoff ~~frequency~~ wavenumber of the respective low-pass filter (Fig. 9(b)). For the lowest gate at height of 10 m, the fitting procedure estimated $\alpha = 5.08$ and ~~$f_{Th} = 0.14$ Hz~~ $k_{Th} = 0.065$ m^{-1}, while for the highest range gate at height of 60 m $\alpha = 4.16$ and ~~$f_{Th} = 0.16$ Hz~~ $k_{Th} = 0.066$ m^{-1}.

~~Results of the correction procedure applied to the SLTEST dataset are shown in Fig. 11. It is noteworthy to observe that the fitting of the LiDAR spectra allows detecting the typical decrease in frequency of the energy peak with increasing height (reported with black triangles in Fig. 11(b)), which is connected with the increase of the integral length scale The correction of the LiDAR spectra keeps unaltered the energy content of the large energy-containing turbulent structures, while a significant correction is performed within the inertial sub-range to improve accuracy in the estimate of the turbulent statistics.~~

Since the correction procedure is based on two consecutive best-fit operations, the robustness of the model is assessed for each LiDAR gate through the R-square value of the respective fitting procedure. ~~Regarding the fitting of the LiDAR spectra with~~

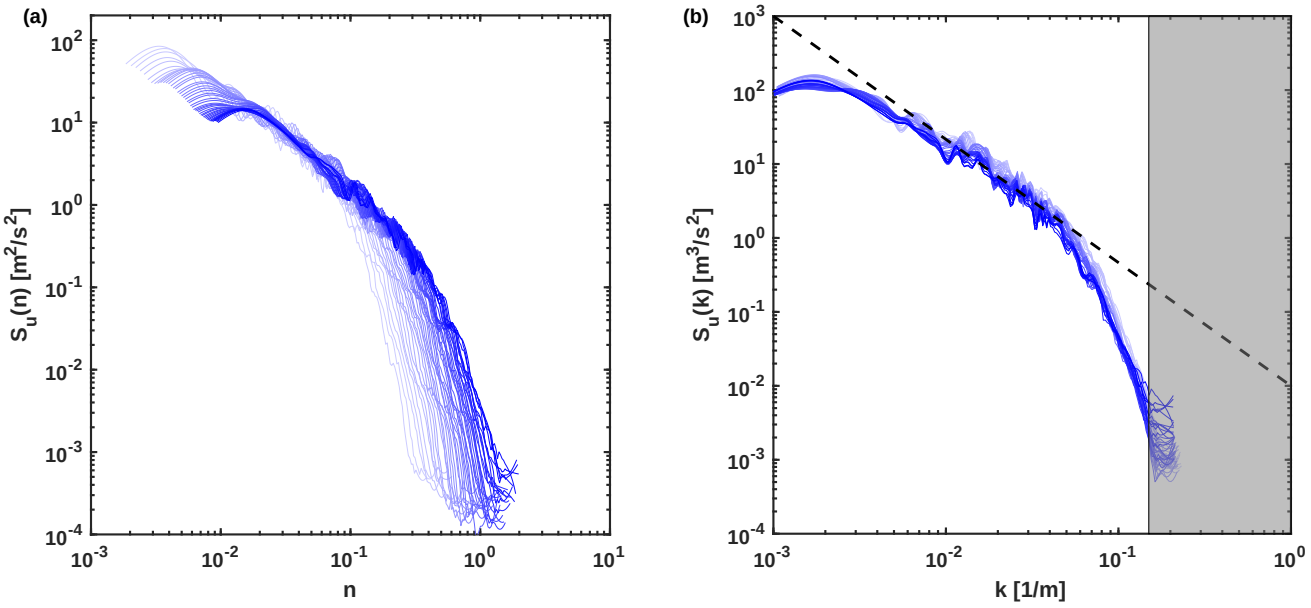

Figure 8. Velocity spectra for the SLTEST dataset at different heights: **(a)** spectra as a function of the reduced frequency, n; **(b)** spectra as a function of the wavenumber, k. Line color is darker with increasing height. The black dashed line represents the $-5/3$ slope. In (b), the shaded area covers the noisy part of the velocity spectra.

~~the Kaimal model of Eq. 1, the R-square value is plotted in Fig. 11(a) for all the heights and available datasets.~~ All the datasets generally show a very good agreement between experimental data and the ~~Kaimal~~ spectral model, i.e. $0.82 \leq R^2 \leq 0.98$, with the SLTEST dataset showing the highest level of agreement ($R^2 \geq 0.96$). ~~To quantify~~ Accuracy in modeling the actual energy damping due to the LiDAR measuring process through the low-pass filter of Eq. 9 is quantified through the R-square value of the fitting procedure of the experimental energy damping, φ_*^2, with the analytical model of Eq. 9. The R-square values result to be always larger than 88%, corroborating the good approximation for the proposed model. ~~of each fitted function is plotted in Fig. 11(b).~~

The proposed spectral correction of the LiDAR measurements is now applied to all the ~~selected~~ datasets collected at the Celina and SLTEST sites (see Table 2). As explained in §2, the first step of the proposed procedure consists in fitting each velocity spectrum with the ~~Kaimal~~ spectral model of Eq. 1. In the right column of Fig. 10, the results of this operation are reported for all the datasets of the SLTEST and Celina field campaigns. The ~~Kaimal~~ spectral model (depicted with a red line) has been fitted on the uncorrected LiDAR spectrum (blue lines) using a cutoff wavenumber, k_{Th}, estimated for each velocity signal using the iterative procedure illustrated in Fig. 1. In the figures, line colors become darker with increasing height. For the sake of clarity, the fitted Kaimal spectrum is only shown for the highest LiDAR range gate.

The second step of the correction procedure consists in approximating the LiDAR-to-Kaimal spectral ratio with the low-pass filter of Eq. 9. Firstly, the energy ratio is quantified for each LiDAR range gate, as reported in the left column of Fig. 10.

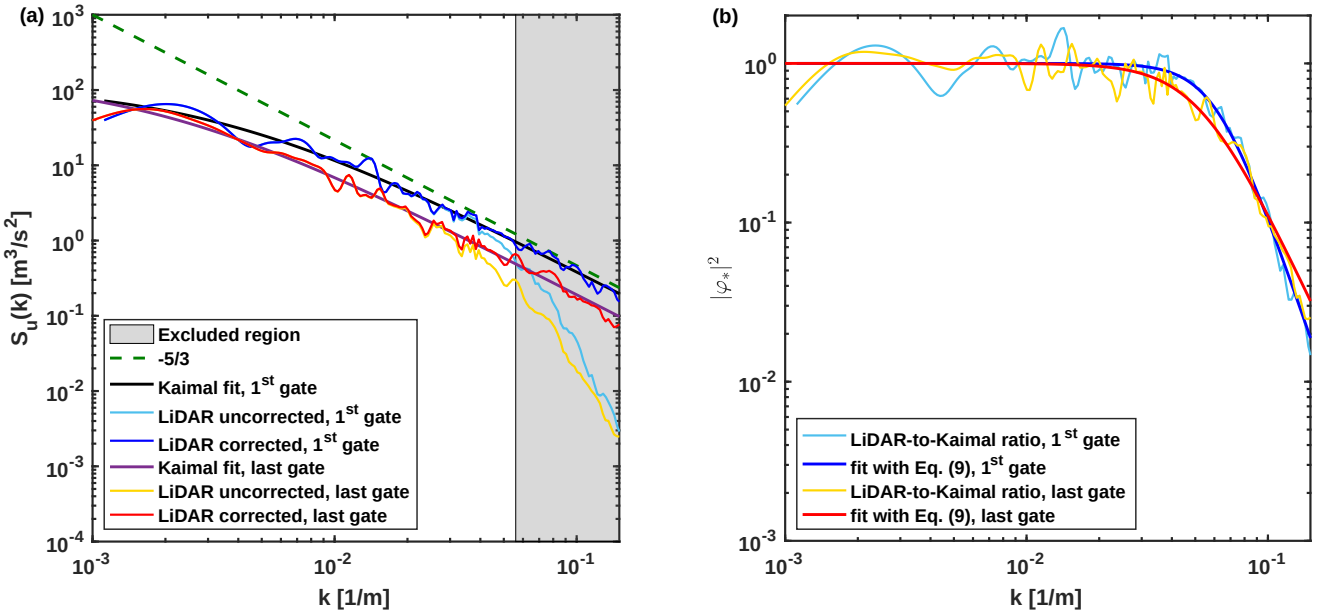

Figure 9. LiDAR velocity signals from the SLTEST dataset acquired at $z = 10$ m (first gate, dark and light blue lines) and $z = 60$ m (last gate, red and yellow lines): **(a)** correction of the LiDAR spectra; **(b)** ratio between LiDAR and Kaimal spectra, φ_*^2, and low-pass filter fitted with Eq. (9).

We can observe that the ratio always settles about the unit at the lowest range of the spectral domain, while it monotonically reduces from the cutoff ~~frequency~~ wavenumber towards the Nyquist ~~frequency~~ wavenumber, which is an effect of the LiDAR measuring process. By plotting $|\varphi_*|^2$ as a function of ~~$(f/f_{Th})^\alpha$~~ $(k/k_{Th})^\alpha$, ~~a quasi self-similar behavior is observed among the various range gates, which represents a further assessment of the accuracy of the proposed correction procedure.~~ all the estimated transfer functions practically collapse on the same curve for measurements collected at different heights. The latter is then compared with the analogous of Eqs. 5 and 6.

As last step, to retrieve the corrected LiDAR velocity spectra, the original spectrum is divided by the modeled correction function, $|\tilde{\varphi}|^2$ (Eq. 10). These corrected LiDAR velocity spectra are reported on the right column of Fig. 10, where we can observe that the $-5/3$ slope of the inertial sub-range is always recovered. The LiDAR spectra corrected with the models of Eq. 5 and 6 are also reported in order to highlight the improved accuracy achieved through the proposed method. In particular, it is observed that the existing models of Eqs. 5 and 6 always under-estimate the spectral energy attenuation; thus, for the actual choices of gate length and sampling rates, a data-driven approach is preferred to correct the LiDAR smoothing effect.

The corrected variance of the LiDAR velocity signals is compared with the respective quantity calculated for the raw LiDAR data in Fig. 11(a). As expected, the wall-normal profile of the variance calculated as integral of the de-convoluted spectrum is considerably larger than the respective value obtained from the convoluted spectrum, indicating that the underestimation related to the spatial averaging is significant. To quantify the effects of the spectral correction on the LiDAR data, the relative

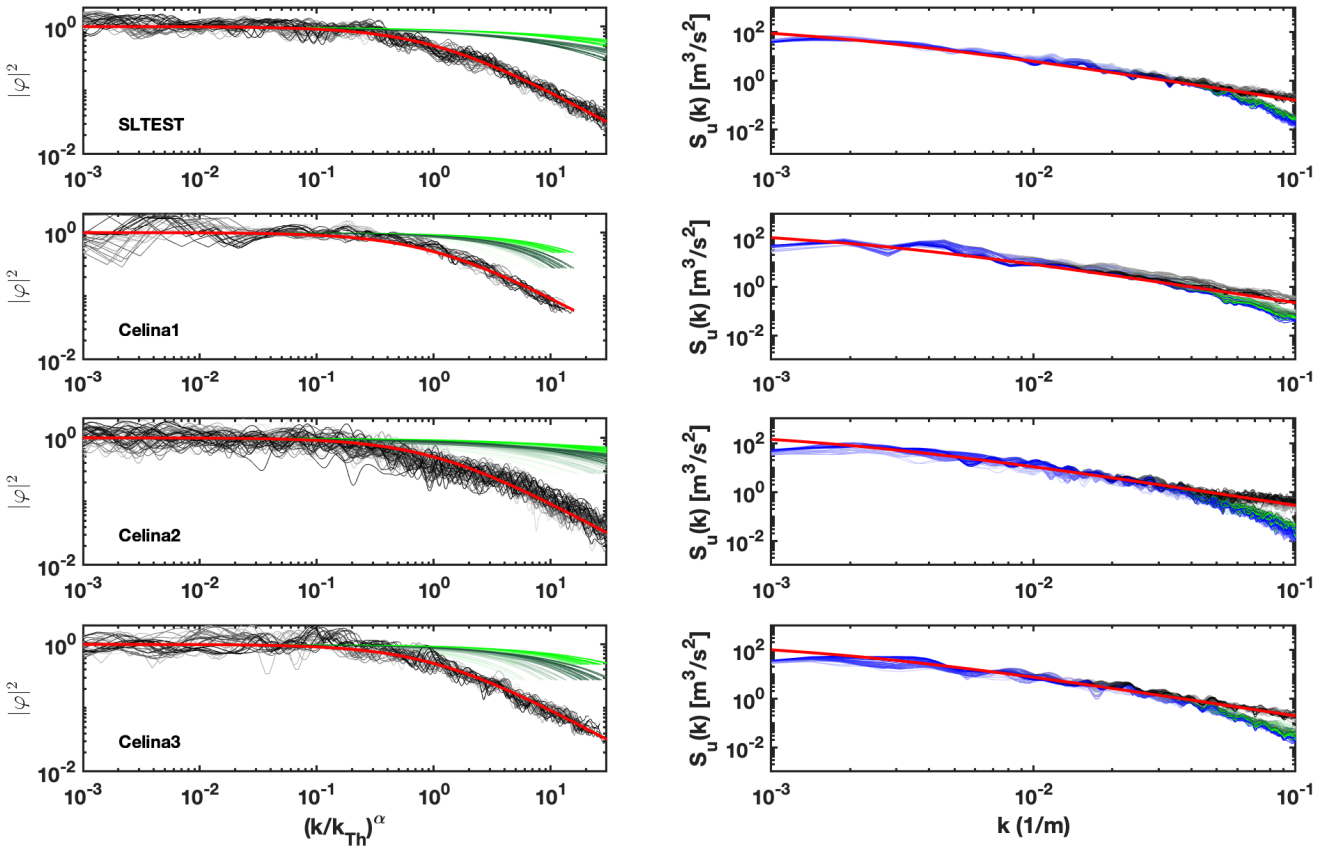

Figure 10. Correction of the LiDAR spectra. Left column: black lines are φ_*^2, the red line is the fitted low-pass filters of Eq. (9) for the highest range gate. Dark and light green lines represent the ~~convolution~~ transfer function predicted by Eqs. (5) and (6). Right column: blue lines are raw LiDAR spectra, dark and light green lines are LiDAR spectra corrected with Eqs. (5) and (6), respectively, the red line is the fitted Kaimal spectrum for the highest range gate and black lines are the LiDAR spectra corrected with the proposed procedure of Fig. 1. Line colors become darker with increasing height.

percentage increment of variance is calculated from the smallest frequency up to the noise-free high-frequency content as in Cheynet et al. (2017):

$$\epsilon_{\%} = \frac{\sigma_C^2 - \sigma_U^2}{\sigma_C^2} \cdot 100, \tag{20}$$

where σ_C^2 and σ_U^2 are the corrected and uncorrected, respectively, streamwise velocity variance. The parameter $\epsilon_{\%}$ is reported as a function of height in Fig. 11(b). The underestimation in the velocity variance through the LiDAR measurements seems to change with the wall-normal location for the SLTEST dataset and the highest portion of Celina1 ($z > 30$m); for the remaining datasets, the percentage error does not change with height. To clarify this aspect, in the next section we will ~~leverage synthetic turbulent velocity signals to better understand the variability of the LiDAR averaging effect in relation with the size of turbulent~~

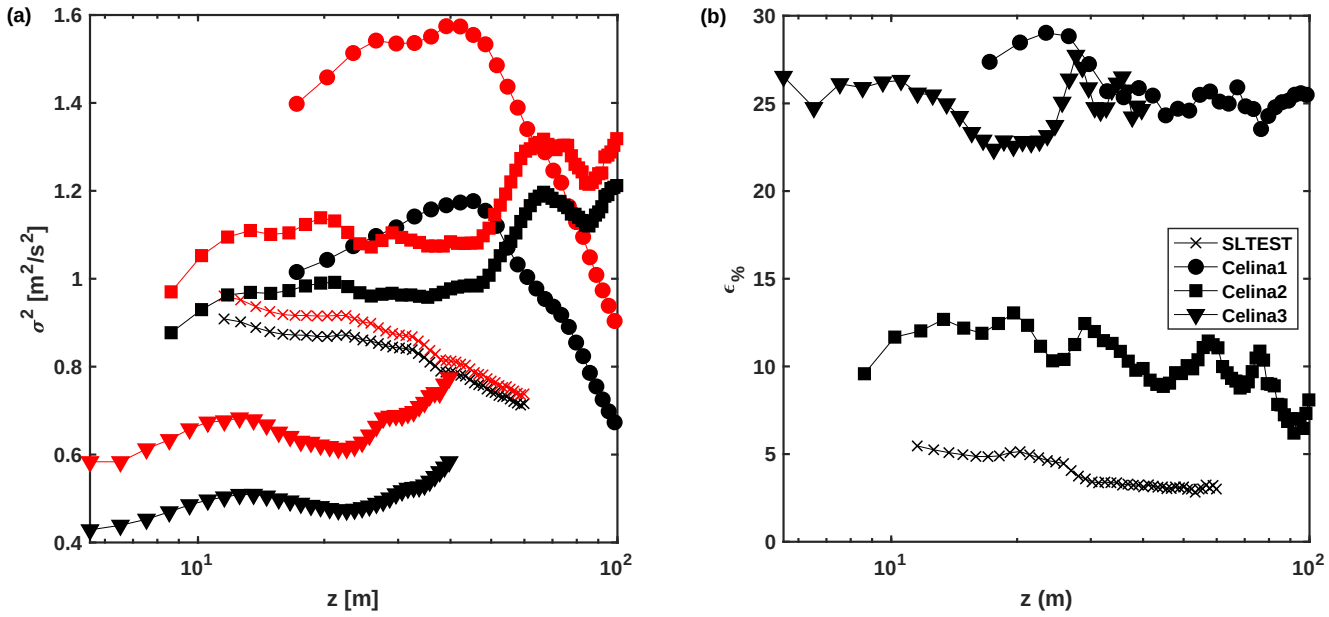

Figure 11. Correction of the second-order statistics: **(a)** Variance before (black) and after (red) the LiDAR spectral correction; **(b)** percentage increment of the velocity variance ($\epsilon_{\%}$) achieved with the LiDAR spectral correction.

~~structures crossing the probe~~ investigate the variability of the effects of the LiDAR spatial averaging for different mean wind speed, standard deviation and sampling height.

We now focus on the variability of the parameters of the low-pass filter of Eq. 9 among the various datasets. Median and interquartile (IQ) range calculated over the height for the various datasets are reported in Table 3 for both order, α, and cutoff wavenumber, k_{Th}, of the low-pass filter of Eq. 9. First, the order of the low-pass filter, α~~, which is reported in Fig.15(a)~~, is found to be roughly constant over the height for the datasets Celina1 and Celina3, while it decreases with height for the

Table 3. Median and inter-quartile (IQ) values of the estimated order, α, and cutoff wavenumber, k_{Th} of the low-pass filter modeling the LiDAR spatial averaging for each dataset.

	α		$k_{Th}l/(2\pi)$	
	Median	IQ Range	Median	IQ Range
SLTEST	4.898	0.358	0.176	0.008
Celina1	2.198	0.163	0.144	0.021
Celina2	4.455	0.653	0.163	0.027
Celina3	2.579	0.422	0.152	0.030

SLTEST and Celina2 datasets. Among the various datasets analyzed, the filter order α has values from 2.2 up to 4.9, a variation entailing limited effects in the correction of the spatial averaging on the LiDAR measurements (not shown here for the sake of brevity). The mean IQ range of α among the various datasets is 0.399. The cutoff ~~frequency~~ wavenumber of the low-pass filter, ~~f_{Th}~~ k_{Th}, is practically constant with height (mean IQ range of 0.022) and has a mean value among the various datasets of: $k_{Th}l/(2\pi)$ =0.163. ~~as shown in Fig. 15(b). In Fig. 15(c), the equivalent cutoff wavelength, λ_{Th} (obtained via Taylor frozen hypothesis) is reported as ratio of the gate length.~~

6 ~~Assessment of the correction procedure through synthetic velocity signals~~ Variability in spatial filtering with mean wind speed, turbulence intensity and sampling height

~~To better understand the importance of the filter order, α, and the cutoff frequency, f_{Th} in Eq. 10, a turbulent synthetic signal is generated, by using a sampling frequency $f_S = 20$ Hz, from the inverse Fast Fourier Transform of a Kaimal-like spectrum (Eq. 1) with $A_f = 10$ m^{2}s^{-1}, $B_f = 20$ s, and providing random phases to the various spectral contributions. The generated time series consists of 36,000 samples evenly spaced in time.~~

~~This synthetic velocity signal is convoluted in the frequency domain with Eq. 10 where the order, α, and the cutoff frequency, f_{Th}, are varied within the intervals $(\alpha, f_{Th}/f_S) = [2,5] \times [0.005, 0.25]$. The energy spectra obtained from the convolution of the synthetic signal with the various low-pass filters obtained by using the extrema of the above-mentioned ranges for α and f_{Th}/f_S are reported in Fig. 16(a), while the respective low-pass filters are depicted in Fig. 16(b). It is evident that the largest deviation from the spectrum of the original synthetic signal is associated with the minimum value of the cutoff frequency (red and cyan lines in Figs. 16(a) and (b)). On the other hand, the filter order produces a secondary effect on the spectral damping, namely a faster damping with increasing frequencies is observed with higher filter orders. To couple damping effects of both cutoff frequency and order of the low-pass filter, the percentage reduction of variance, which is calculated through Eq. 20, is reported in Fig. 16(c). This color map corroborates that the largest variability in the damping of the energy spectra occurs with variations of the cutoff frequency, while the gradient in the vertical direction, namely with variations of α, is practically negligible. Specifically, for a cutoff frequency interval ranging from 0.5% to 25% of the sampling rate, the corresponding energy reduction varies from 45% down to 5%, which is in agreement with the experimental data reported in Fig. 14(b). Therefore, for the correction of the spectral damping of the LiDAR velocity signals, the main parameter to be tuned for the correction procedure is the cutoff frequency of the low-pass filter.~~

~~We now attempt to interpret the variability in the damping of the velocity variance as a function of height observed from the experimental datasets, as it has been reported in Fig. 14(b).~~

To investigate effects of the spatial averaging on wind LiDAR measurements for different mean wind speed, turbulence intensity, and sampling height of the velocity signals, synthetic turbulent velocity spectra are generated using the spectral model of Eq. 1, while the energy damping connected with the LiDAR measuring process is estimated through Eq. 9 by using a filter order $\alpha = 3$ and $(k_{Th}l) = 0.95$, in analogy to the respective experimental values reported in Table 3.

Within the inertial sublayer, namely for heights smaller than about 30% of the surface layer height (Marusic et al. , 2013), the mean streamwise velocity for near-neutral stability conditions can be modeled through the following logarithmic law (Monin and Obukhov , 1954; Stull , 1988):

$$U = \frac{u_\tau}{\kappa} \log\left(\frac{z}{z_0}\right), \tag{21}$$

where $\kappa = 0.41$ is the Von Kármán constant. Furthermore, we should expect a logarithmic decrease in the velocity variance with increasing wall-normal distance (Townsend , 1976), as follows:

$$\frac{\sigma^2}{u_\tau^2} = H_1 - G_1 \log\left(\frac{z}{\delta}\right), \tag{22}$$

where δ is the surface layer height, while the parameters H_1 and G_1 might be dependent on the characteristics of the specific boundary layer flow under investigation. Previous field campaigns performed at the SLTEST site have quantified them as follows: $H_1 = 2.14$ and $G_1 = 1.33$ (Marusic et al. , 2013).

According to the spectral model of Eq. 1, the velocity variance can be obtained by integrating S_u in the spectral domain, which leads to:

$$\frac{\sigma^2}{u_\tau^2} = \int_0^\infty \frac{A}{(1+Bn)^{5/3}}\, dn = \frac{3}{2}\frac{A}{B}, \tag{23}$$

where A and B vary with the sampling height.

~~To generate synthetic velocity signals throughout the boundary layer height similar to those observed from the experimental datasets, the vertical profile of B_f has been selected equal to that measured for the SLTEST dataset, which is related to the spectral peak reported with black empty circles in Fig. 11(b). Using the values of H_1, G_1 provided by~~ Marusic et al. (2013)~~, the logarithmic profile of variance is estimated from Eq. 21 over the height range $z/\delta \in [0.1 \quad 1]$. Finally, A_f is calculated from Eq. 22.~~

~~The convolution of the synthetic velocity signals is performed by using $\alpha = 3$ and $f_{Th} \in [0.05, \quad 0.15]$ Hz. The sampling rate is assumed equal to 20 Hz, while the total number of samples is $40,000$. The variance associated with the low-pass filtered velocity signals is reported as a function of height and for the various cutoff frequencies in Fig. 17(a). In agreement with the results reported in Fig. 16, a more severe damping is inferred to the synthetic velocity signals with reducing cutoff frequency. Furthermore, a lower cutoff frequency entails a more marked departure of the variance trend as a function of height from the expected logarithmic law, which also extends to higher heights.~~

~~By calculating the percentage reduction of the variance, $\epsilon_\%$, through Eq. 20, it is observed that the damping in the variance due to the LiDAR measuring process typically decreases with height until a certain asymptotic error is achieved for heights between 0.3δ-0.4δ. It is interesting that this feature singled out through the analysis of the synthetic velocity signals is very similar to that observed in Fig. 14(b) for the SLTEST dataset, for which the surface layer height, δ has been estimated between 60 m and 100 m from previous works~~ (Hutchins and Marusic , 2007; Metzger et al. , 2007; Marusic and Hutchins , 2008)~~. A similar~~

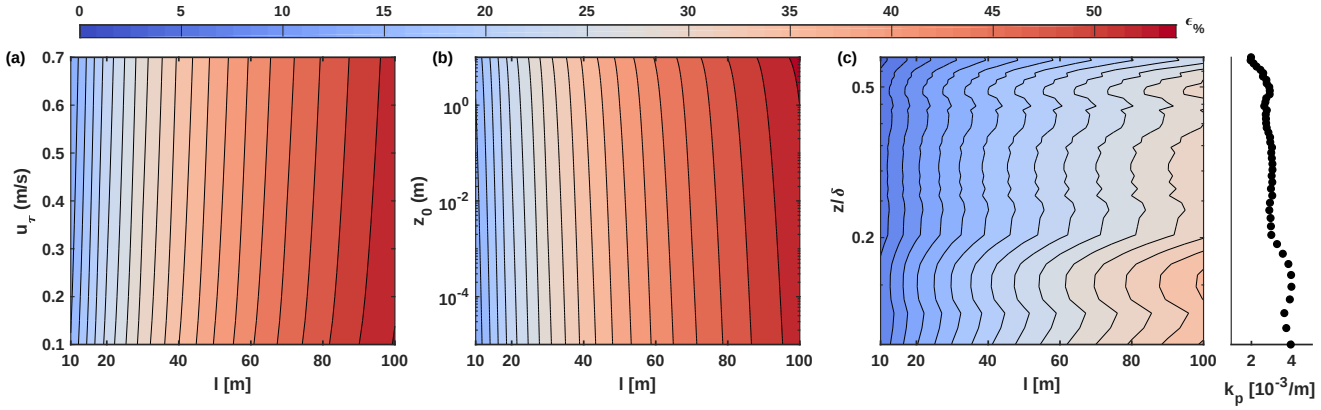

Figure 12. Variation of the percentage variance damping, $\epsilon_{\%}$ connected with the LiDAR spatial averaging for different probe lengths and wind conditions: **(a)** variability with the friction velocity, u_τ; **(b)** variability with the aerodynamic roughness length, z_0; **(c)** variability with sampling height, z. The side panel of (c) reports the vertical profile of the parameter k_p estimated for the SLTEST dataset.

~~trend is also observed for the dataset Celina1 even though it exhibits a larger variance error (nearly 25%). For the remaining datasets, a roughly constant percentage error has been calculated, which might correspond to the region with asymptotic $\epsilon_{\%}$ values observed in Fig. 17(b).~~

The first analysis is performed by varying the friction velocity, u_τ, within the range between 0.1 m s^{-1} and 0.7 m s^{-1} with a step of 0.05 m s^{-1}, while keeping fixed the sampling height $z/\delta = 0.3$ ($B = 33$ (Kaimal et al. , 1972)), and $z_0 = 10^{-4}$ m. This study aims to investigate variation in LiDAR spatial averaging for mean wind speed within the range $U \in [3, 23]$ m s^{-1}, while keeping unchanged the turbulence intensity (TI = $\sigma/U = 6.29\%$ at $z/\delta = 0.3$). The velocity standard deviation varies linearly with u_τ within the range $\sigma = [0.19, 1.35]$ m s^{-1} (Eq. 22), and the respective values of the parameter A are calculated from Eq. 23. The probe length, l, is varied from 10 m up to 100 m with a step of 10 m.

The parameter $\epsilon_{\%}$, which is defined in Eq. 20, is used to quantify the effects of the LiDAR spatial averaging on the variance of the wind velocity. In Fig. 12(a), it is observed that, as expected, $\epsilon_{\%}$ increases with increasing probe length, which indicates that the probe length is the main root cause for the spatial averaging. Furthermore, it is noteworthy that for a given value of l, $\epsilon_{\%}$ decreases with increasing u_τ and, thus, mean wind speed, U. Indeed, by fixing the probe length, the cutoff wavenumber, k_{Th}, representing the spatial averaging is, in turn, fixed while the reduction of $\epsilon_{\%}$ with increasing U can be explained in the perspective of the Taylor frozen-turbulence hypothesis (Taylor , 1938). In other terms, with increasing U, a turbulent spectrum will shift towards lower wavenumbers (denominator in Eq. 1) and, thus, reducing the percentage of the spectral energy that is filtered for wavenumbers larger than k_{Th}.

The second test case, whose results are reported in Fig. 12(b), is performed by varying the aerodynamic roughness length within the range: $z_0 = [10^{-5}, 10]$ m, while keeping fixed u_τ= 0.5 m s^{-1}, and sampling height $z/\delta = 0.3$ (B=33). In this case, variations of z_0 affect directly the mean velocity (Eq. 21), while the velocity standard deviation is unchanged (Eq. 22). Therefore, this study can be considered as a test to investigate the effects on the LiDAR spatial averaging due to variation of

the wind turbulence intensity, which might be connected to different site terrain roughness, variations of wind direction, and atmospheric stability regime. Specifically, for a fixed probe length, an increase of aerodynamic roughness length leads to a reduction of the mean velocity for a given height and friction velocity, and a shift of the turbulent spectrum towards higher wavenumbers and, in turn, enhanced effects of the spatial averaging on the LiDAR measurements.

The last case study is performed for a given wind condition, namely with $u_\tau = 0.5$ m s^{-1} and $z_0 = 10^{-4}$m, and by varying the measurement height within the range $z/\delta = [0.1, 0.6]$. The vertical variability of the parameter $B = [65,\ 228]$ has been selected equal to that measured for the SLTEST dataset, and the respective values of the wavenumber of the spectral peak, k_p, are reported in the side panel of Fig. 12(c). For each height, the velocity variance is calculated via Eq. 22 and the corresponding value of A is obtained through Eq. 23. The resulting percentage reduction of variance is plotted in Fig. 12(c). For a fixed probe length, it is observed that $\epsilon_{\%}$ generally decreases with height in a way similar to what observed experimentally in Fig. 11(b), and the variations of $\epsilon_{\%}$ are strongly dependent on the variations of the parameter k_p. In other words, with increasing height, the general reduction of k_p leads to a smaller percentage of the spectral energy of the velocity signal present for wavenumbers larger than k_{Th}, which is fixed once the LiDAR probe length is selected. Therefore, smaller effects of the LiDAR spatial averaging occur with increasing height for a given wind condition and probe length.

7 Conclusions

Pulsed Doppler wind LiDAR technology is gradually achieving compelling technical specifications, such as ~~range gates~~ probe lengths smaller than 20 m and sampling frequencies higher than 1 Hz, which are instrumental to investigate atmospheric turbulence with length scales typical of the inertial sub-range. However, the emission of a laser pulse over the ~~range gate~~ probe volume to measure the radial velocity entails a spatial smoothing process leading to damping on the measured variance of the velocity fluctuations. Existing models propose to correct the effects of spatial averaging on LiDAR measurements through a deconvolution procedure where the smoothing function represents the energy distribution of the laser pulse over the ~~range gates~~ probe length. According to previous works, and also confirmed through this study, these deconvolution methods have limited accuracy in correcting the LiDAR velocity fluctuations.

In this work, we have proposed to correct the measured LiDAR velocity signals by inverting the effects of a low-pass filter representing the energy damping on the velocity fluctuations due to the LiDAR measuring process. The filter characteristics, namely order and cutoff ~~frequency~~ wavenumber, are directly estimated from the spectrum of the LOS velocity under investigation. Specifically, the spectrum of the LiDAR velocity signal is fitted through the Kaimal spectral model for streamwise turbulence only for ~~frequencies~~ wavenumbers lower than a cutoff value for which the slope of the LiDAR velocity spectrum is observed to deviate from the expected $-5/3$ slope typical of the inertial sub-range. The ratio between the LiDAR and the Kaimal spectra is then fitted with the analytical expression of a low-pass filter to estimate order and cutoff ~~frequency~~ wavenumber. An iterative procedure is proposed to estimate order and cutoff wavenumber of the low-pass filter. The modeled low-pass filter is then reverted on the LiDAR data to correct the LiDAR measurements and produce more accurate second-order statistics and spectra of the streamwise wind velocity.

For this study, the proposed method for correction of the LiDAR data has been applied to datasets collected during three different field campaigns and for one dataset the procedure has been assessed against simultaneous and co-located sonic anemometer data. For this case, it has been shown that the proposed procedure allows us to correct the second-order statistics of the LiDAR data to estimate a velocity variance comparable to that measured by a sonic anemometer.

This study has shown that it is challenging to determine a priori the cutoff ~~frequency~~ wavenumber and order of the low-pass filter representing the energy damping of the LiDAR measuring process for a given LiDAR system, LiDAR settings, atmospheric and wind conditions. Therefore, we rather propose to determine the parameters of the low-pass filter on a case-by-case basis by applying the proposed procedure on the LiDAR signal under investigation.

To better understand the role of the cutoff ~~frequency~~ wavenumber and order of the low-pass filter representing the LiDAR energy damping, further analysis has been conducted on synthetic turbulent velocity ~~signals~~ spectra. This analysis has been performed by varying mean wind speed, turbulence intensity, and sampling height. This analysis has shown that the main parameter for efficiently correct the LiDAR energy damping is the cutoff ~~frequency~~ wavenumber of the low-pass filter, which is mainly affected by the probe length and the energy distribution of the laser pulse over the probe volume, while the velocity statistics are weakly affected by the filter order. Furthermore, the results have confirmed that for a given probe length, effects of spatial averaging are enhanced with decreasing wind speed, smaller integral length scale and, thus, for a lower sampling height. ~~Subsequently, investigating effects of the LiDAR energy damping on synthetic turbulent velocity signals characterized by a logarithmic reduction of the variance with decreasing height from the ground, it has been shown that the LiDAR energy damping leads to a departure of the variance as a function of height from the expected logarithmic trend, while achieving an asymptotic percentage error with increasing heights. As expected, the energy damping is enhanced with reducing cutoff frequency of the low-pass filter and it is extend to a higher altitudes. Summarizing, the proposed procedure allows achieving efficient corrections of the second order statistics and spectra of the LiDAR measurements by inverting the effects of a low-pass filter, whose characteristics are directly estimated from the LiDAR data. However, further investigations with different LiDAR systems, LiDAR settings, such as range gate and accumulation time, and atmospheric wind conditions are needed to be able to predict a priori the correction parameters.~~

Acknowledgements. This work was supported by the National Science Foundation (NSF) CBET grant # 1705837, program manager Dr. Ronald Joslin. The authors are thankful to Eric Pardyjak, Marc Calaf and Sebastian Hoch for their support during the SLTEST experiment, and to Julie K. Lundquist for leading the XPIA field campaign.

References

Balasubramaniam, B. J.: Nature of turbulence in wall bounded flows, Ph.D. Thesis, University of Illinois at Urbana-Champaign, 2005.

Banakh, V. A. and Werner C.: Computer simulation of coherent Doppler lidar measurement of wind velocity and retrieval of turbulent wind statistics, Opt. Eng., 44(7), 071205, https://doi.org/10.1117/1.1955167, 2005.

Banerjee, T., Katul, G. G., Salesky, S. T., and Chamecki, M.: Revisiting the formulations for the longitudinal velocity variance in the unstable atmospheric surface layer, Q. J. R. Meteor. Soc., 141, 1699–1711, https://doi.org/10.1002/qj.2472, 2015.

Bodini, N., Zardi, D., and Lundquist, J. K.: Three-dimensional structure of wind turbine wakes as measured by scanning lidar, Atmos. Meas. Tech., 10, 2881–2896, https://doi.org/10.5194/amt-10-2881-2017, 2017.

Carbajo Fuertes, F., Iungo, G. V., and Porté-Agel, F.: 3D turbulence measurements using three synchronous wind lidars: validation against sonic anemometry, J. Atmos. Oceanic Technol., 31, 1549-1556, https://doi.org/10.1175/JTECH-D-13-00206.1, 2014.

Cheynet, E., Jakobsen J., Snæbjörnsson J., Mann J., Courtney M., Lea G., and Svardal B.: Measurements of surface-layer turbulence in a wide Norwegian fjord using synchronized long-range Doppler wind lidars, Remote Sens., 9, 977, https://doi.org/10.3390/rs9100977, 2017.

Choukulkar, A., Brewer, W. A., Sandberg, S. P., Weickmann, A., Bonin, T. A., Hardesty, R. M., Lundquist, J. K., Delgado, R., Iungo, G. V., Ashton, R., Debnath, M., Bianco, L., Wilczak, J. M., Oncley, S., and Wolfe, D.: Evaluation of single and multiple Doppler lidar techniques to measure complex flow during the XPIA field campaign, Atmos. Meas. Tech., 10, 247-264, https://doi.org/10.5194/amt-10-247-2017, 2017.

D'Errico, J.: Inpaint nans, MATLAB Central File Exchange, 2004.

Debnath, M., Iungo, G. V., Brewer, W. A., Choukulkar, A., Delgado, R., Gunter, S., Lundquist, J. K., Schroeder, J. L., Wilczak, J. M., and Wolfe, D.: Assessment of virtual towers performed with scanning wind lidars and Ka-band radars during the XPIA experiment, Atmos. Meas. Tech., 10, 1215-1227, https://doi.org/10.5194/amt-10-1215-2017, 2017a.

Debnath, M., Iungo, G. V., Ashton, R., Brewer, W. A., Choukulkar, A., Delgado, R., Lundquist, J. K., Shaw, W. J., Wilczak, J. M., and Wolfe, D.: Vertical profiles of the 3-D wind velocity retrieved from multiple wind lidars performing triple range-height-indicator scans, Atmos. Meas. Tech., 10, 431-444, https://doi.org/10.5194/amt-10-431-2017, 2017b.

Debnath, M.: Evolution within the atmospheric boundary layer of coherent structures generated by wind turbines: LiDAR measurements and modal decomposition, Ph.D. thesis, The University of Texas at Dallas, USA, 2018.

Eberhard, W. L., Cupp, R. E., and Healy, K. R.: Doppler lidar measurement of profiles of turbulence and momentum flux, J. Atmos. Oceanic Technol., 6, 809-819, https://doi.org/10.1175/1520-0426(1989)006<0809:DLMOPO>2.0.CO;2, 1989.

Emeis, S., Harris, M., and Banta, R. M: Boundary-layer anemometry by optical remote sensing for wind energy applications, Meteorol. Z., 16, 337-347, https://doi.org/10.1127/0941-2948/2007/0225, 2007.

Foken, T., Göockede, M., Mauder, M., Mahrt, L., Amiro, W., and Munger, W.: Post-field data quality control, Handbook of Micrometeorology, Springer Netherlands, Dordrecht, 181-208, https://doi.org/10.1007/1-4020-2265-4_9, 2004.

Frehlich, R. and Kelley, N.: Measurements of wind and turbulence profiles with scanning Doppler lidar for wind energy applications, IEEE J. Sel. Top. Appl., 1 (1), 42-47, https://doi.org/10.1109/JSTARS.2008.2001758, 2008.

Held, D.P. and Mann, J.: Comparison of methods to derive radial wind speed from a continuous-wave coherent lidar Doppler spectrum, Atmos. Meas. Tech., 11(11), 6339-6350, https://doi.org/10.5194/amt-11-6339-2018, 2018.

Hu, R., Yang, X. I. A., and Zheng, X.: Wall-attached and wall-detached eddies in wall-bounded turbulent flows, J. Fluid Mech., 885, A30-24, https://doi.org/10.1017/jfm.2019.980, 2019.

Hutchins, N. and Marusic, I.: Evidence of very long meandering features in the logarithmic region of turbulent boundary layers, J. Fluid Mech., 579, 1-28, https://doi.org/10.1017/S0022112006003946, 2007.

Hutchins, N., Chauhan, K., Marusic, I., Monty, J., and Klewicki, J.: Towards reconciling the large-scale structure of turbulent boundary layers in the atmosphere and laboratory, Boundary-Layer Meteorol., 145, 273-306, https://doi.org/10.1007/s10546-012-9735-4, 2012.

International Electrotechnical Commission IEC 61400-1: Wind turbines-part 1: design requirements, 3 Ed., 2007.

Iungo, G. V., Wu, Y. T., and Porté-Agel, F.: Field measurements of wind turbine wakes with lidars, J. Atmos. Oceanic Technol., 30, 274-287, https://doi.org/10.1175/JTECH-D-12-00051.1 , 2013.

Kaimal, J. C., Wyngaard, J. C., Izumi, Y., and Coté, O. R.: Spectral characteristics of surface layer turbulence, Q. J. R. Meteorol. Soc., 98, 563-589, https://doi.org/10.1002/qj.49709841707, 1972.

Kaimal, J. C. and Finnigan, J. J.: Atmospheric boundary layer flows: their structure and measurement, Oxford University Press, New York, 1994.

Kristensen, L., Kirkegaard, P., and Mikkelsen T.: Determining the velocity fine structure by a laser, Technical University of Denmark, Lyngby, Denmark, 33, 2011.

Kunkel, G. J. and Marusic, I.: Study of the near-wall-turbulent region of the high-Reynolds-number boundary layer using an atmospheric flow, J. Fluid Mech., 548, 375-402, https://doi.org/10.1017/S0022112005007780, 2006.

Lindelöw, P.: Fiber based coherent lidars for remote wind sensing, Ph.D. thesis, Technical University of Denmark, Lyngby, Denmark, 2008.

Liu, H. Y., Bo, T. L., and Liang, Y. R.: The variation of large-scale structure inclination angles in high Reynolds number atmospheric surface layers, Phys. Fluids, vol. 29, 035104, https://doi.org/10.1063/1.4978803, 2017.

Lundquist, J. K., Wilczak, J. M., Ashton, R., Bianco, L., Brewer, W. A., Choukulkar, A., Clifton, A., Debnath, M., Delgado, R., Friedrich, K., Gunter, S., Hamidi, A., Iungo, G. V., Kaushik, A., Kosovic, B., Langan, P., Lass, A., Lavin, E., Lee, J. C. Y., McCaffrey, K. L., Newsom, R., Noone, D. C., Oncley, S. P., Quelet, P. T., Sandberg, S. P., Schroeder, J. L., Shaw, W. J., Sparling, L., Martin, C. S., Pe, A. S., Strobach, E., Tay, K., Vanderwende, B. J., Weickmann, A., Wolfe, D., and Worsnop, R.: Assessing state-of-the-art capabilities for probing the atmospheric boundary layer: the XPIA field campaign, B. Am. Meteorol. Soc., 98, 289-314, https://doi.org/10.1175/BAMS-D-15-00151.1, 2017.

Mann, J.: The spatial structure of neutral surface-layer atmospheric turbulence, J. Fluid Mech., 273, 141–168, https://doi.org/10.1017/S0022112094001886, 1994.

Mann, J., Cariou, P., Courtney, M. S., Parmantier, R., Mikkelsen, T. , Wagner, R. , Lindelow, P., Sjoholm, M., and Enevoldsen, K. : Comparison of 3D turbulence measurements using three staring wind lidars and a sonic anemometer, Meteorol. Z., 18(2), 135-140, https://doi.org/10.1127/0941-2948/2009/0370, 2009.

Marusic, I. and Hutchins, N.: Study of the log-layer structure in wall turbulence over a very large range of Reynolds number, Flow Turbul. Combust., 81, 115-130, https://doi.org/10.1007/s10494-007-9116-0, 2008.

Marusic, I., Monty, J. P., Hultmark, M., and Smits, A. J.: On the logarithmic region in wall turbulence, J. Fluid Mech., 716, R3, https://doi.org/10.1017/jfm.2012.511, 2013.

Meneveau, C. and Marusic, I.: Generalized logarithmic law for high-order moments in turbulent boundary layers, J. Fluid Mech., 719, 1–11, https://doi.org/10.1017/jfm.2013.61, 2013.

Metzger, M. M. and Klewicki, J. C.: A comparative study of near-wall turbulence in high and low Reynolds number boundary layers, Phys. Fluids, 13, 692-701, https://doi.org/10.1063/1.1344894, 2001.

Metzger, M. M., McKeon, B. J., and Holmes, H.: The near-neutral atmospheric surface layer: turbulence and non-stationarity, Philos. T. R. Soc. A, 135, 859-876, https://doi.org/10.1098/rsta.2006.1946, 2007.

Mikkelsen, T., Courtney, M., Antoniou, I., and Mann, J.: Wind scanner: a full-scale laser facility for wind and turbulence measurements around large wind turbines, in: Europ. Wind Energy Conf., Brussels, Belgium, 31 March - 3 April 2008, 1, 012018, 2008.

Monin, A. S. and Obukhov, A. M.: Basic laws of turbulent mixing in the surface layer of the atmosphere, Contrib. Geophys. Inst. Acad. Sci. USSR, 24, 163-187, 1954.

Ogata, K.: Modern Control Engineering, 5 Ed., Prentice Hall, Pearson, 2010.

Olesen, H.R., Larsen, S.E., and Højstrup, J.: Modelling velocity spectra in the lower part of the planetary boundary layer, Boundary-Layer Meteorol., 29(3), 285–312, https://doi.org/10.1007/BF00119794, 1984.

Panofsky, H. A. and Dutton J. A.: Atmospheric turbulence, John Wiley & Sons, New York, 1984.

Risan, A., Lund, J.A., Chang, C.Y. and Sætran, L.: Wind in complex terrain-lidar measurements for evaluation of CFD simulations, Remote Sens., 10(1), 59, https://doi.org/10.3390/rs10010059, 2018.

Sathe, A. and Mann, J.: A review of turbulence measurements using ground-based wind lidars, Atmos. Meas. Tech., 6, 3147-3167, https://doi.org/10.5194/amt-6-3147-2013, 2013.

Savitzky, A. and Golay, M. J.: Smoothing and differentiation of data by simplified least squares procedures, Anal. Chem., 36(8), 1627-1639, 1964.

Simiu, E. and Scanlan, R. H.: Wind effects on structures: fundamentals and application to design, 3 Ed., John Wiley, New York, 1996.

Sjöholm, M., Mikkelsen, T., Mann, J., Enevoldsen, K., and Courtney, M.: Spatial averaging-effects on turbulence measured by a continuous-wave coherent lidar, Meteorol. Z. , 18, 281-287, https://doi.org/10.1127/0941-2948/2009/0379, 2009.

Spuler, S.M. and Mayor, S.D.: Scanning eye-safe elastic backscatter lidar at 1.54 μm. J. Atmos. Oceanic Technol. , 22(6), 696-703, https://doi.org/10.1175/JTECH1755.1, 2005.

Stull, R. B.: An introduction to boundary layer meteorology, Springer, Dordrecht, 1988.

Taylor, G. I.: The spectrum of turbulence, P. R. Soc. London, 164, 476–490, 1938.

Townsend, A. A.: The structure of turbulent shear flow, 2nd Ed., Cambridge University Press, 1976.

To, A. C., Moore, J. R., and Glaser, S. D.: Wavelet denoising techniques with applications to experimental geophysical data, Signal Process., 89(2), 144–160, https://doi.org/10.1016/j.sigpro.2008.07.023, 2009.

Weinstein, C.J.: Programs for digital signal processing, IEEE Press New York, 1979

Welch, P. D.: The use of fast Fourier transform for the estimation of power spectra: a method based on time averaging over short, modified periodograms, IEEE T. Acoust. Speech, AU-15, 70-73, https://doi.org/10.1109/TAU.1967.1161901,1967.

Worsnop, R. P., Bryan, G. H., Lundquist, J. K., and Zhang, J. A.: Using large-eddy simulations to define spectral and coherence characteristics of the hurricane boundary layer for wind-energy applications, Boundary-Layer Meteorol., 165(1), 55-86, https://doi.org/10.1007/s10546-017-0266-x, 2017.

Zhan, L., Letizia, S., and Iungo, G. V.: LiDAR measurements for an onshore wind farm: wake variability for different incoming wind speeds and atmospheric stability regimes, Wind Energy, 1-27, https://doi.org/10.1002/we.2430, 2019.